3

AEDC-TR-69-264

Cy. 1

EXPERIMENTAL VERIFICATION OF MAGNET COIL ANALYTICAL MODELS

R. F. Carter
ARO, Inc.

March 1970

This document has been approved for public release and sale; its distribution is unlimited.

VON KÁRMÁN GAS DYNAMICS FACILITY
ARNOLD ENGINEERING DEVELOPMENT CENTER
AIR FORCE SYSTEMS COMMAND
ARNOLD AIR FORCE STATION, TENNESSEE

NOTICES

EXPERIMENTAL VERIFICATION OF MAGNET COIL ANALYTICAL MODELS

R. F. Carter
ARO, Inc.

FOREWORD

The work reported herein was sponsored by the Arnold Engineering Development Center (AEDC), Air Force Systems Command (AFSC), under Program Element 63101F, Project 7778, and Task 777807.

The results of research presented were obtained by ARO, Inc. (a subsidiary of Sverdrup & Parcel and Associates, Inc.), contract operator of AEDC, AFSC, Arnold Air Force Station, Tennessee, under Contract F40600-69-C-0001. The research was conducted during the period from November 1968 to February 1969 under ARO Project Number VJ3921, and the report was submitted for publication on October 29, 1969.

This work was presented as a thesis to the Graduate Council of the University of Tennessee in partial fulfillment of the requirements for the degree Master of Science in May 1969. Appreciation is expressed for the guidance received from Dr. F. M. Shofner of the University of Tennessee Space Institute, Tullahoma, Tennessee, who served as major professor.

This technical report has been reviewed and is approved.

Thomas G. Horn Second Lieutenant, USAF Technical Facility Development Division Directorate of Plans and Technology	Harry L. Maynard Colonel, USAF Director of Plans and Technology

ABSTRACT

In this study of the elastic stresses in thick, strip-wound magnet coils experimental data are compared with theoretical stresses based on three physical models. It is shown that the floating shell model predicts radial dependence of the circumferential stresses produced by the $\vec{J} \times \vec{B}$ body forces better than the monolithic disc or magnetic pressure models.

The fundamental equations relating the magnetic body forces to the stresses in the conductors are derived from first principles. The instrumentation for measuring stresses within magnet windings is described. A survey of several recent magnet stress studies is included.

TABLE OF CONTENTS

LIST OF FIGURES

NOMENCLATURE

a_1	Inside radius of coil
a_2	Outside radius of coil
B	Magnetic induction
B_o	Magnetic induction at geometric center of coil
b	Half length of coil
C	Capacitance
D	Electric displacement
$\vec{e}$	Unit vector
E	Modulus of elasticity; also electromotive force
F	Magnetic force
$F(\alpha,\beta)$	Coil field factor defined in Equation (7)
H	Magnetic field intensity
I	Current per turn of conductor
J	Current density in conductor
K	Constant defined in Equation (32)
L	Inductance of coil
m	Absolute value of the slope of the B_z/B_o versus γ plot
n	Number density of current carrying charges
N	Number of turns in coil
P_m	Magnetic pressure
q	Electric charge
R	Electrical resistance

r	Radial coordinate: also radius at some point in coil
t	Time
u	Radial displacement
v	Velocity
V	Conductor volume
V_o	Capacitor charge voltage
y	Value of ratio B_z/B_o at $\gamma = 1$
z	Distance along axis from geometric center of coil; also axial coordinate
α	Ratio of outer to inner coil radius, a_2/a_1
β	Ratio of coil half length to coil inner radius, b/a_1
γ	Ratio of intermediate radius to coil inner radius, r/a_1
δ	Incremental change
Δ	Incremental change
ε	Unit strain
θ	Circumferential coordinate
λ	Coil space factor
μ	Linear permeability
μ_o	Permeability of free space
ν	Poisson's ratio
σ	Unit stress, also electrical conductivity
τ	Diffusion time constant
Φ	Magnetic flux
ω	Radian frequency

Subscripts

r	Radial direction
z	Axial direction
θ	Circumferential direction

Superscripts

*	Denotes plane strain condition
^	Denotes peak value
→	Denotes vector quantity

CHAPTER I

INTRODUCTION

I. STATEMENT OF PROBLEM

Air core electromagnets are used extensively to generate the high-intensity magnetic fields required in many current research programs. The field attainable with a given magnet is limited by the $\vec{J} \times \vec{B}$ body forces exerted on the windings. This body force (force per volume), gives rise to stresses in the current conductors proportional to the square of the field intensity and may cause mechanical breakdown. A magnet coil may fail by bursting or by localized yielding and subsequent electrical shorting.

A survey of the literature reveals that, although the subject of magnet stresses has been treated in detail [1 through 9][1], quite diverse results are obtained by use of various models which have been assumed. The intent of this study was to establish the most accurate of several models for the calculation of stress distributions within the windings of a widely used type of magnet construction.

The particular magnet construction considered herein is the spirally-wound, cylindrical coil with inside radius a_1, outside radius a_2, and length 2b as depicted in Figure 1. The coil is assumed to be uniformly wound with strip or foil conductor. For generality the coil

---

[1] Numbers in brackets refer to similarly numbered references in the bibliography.

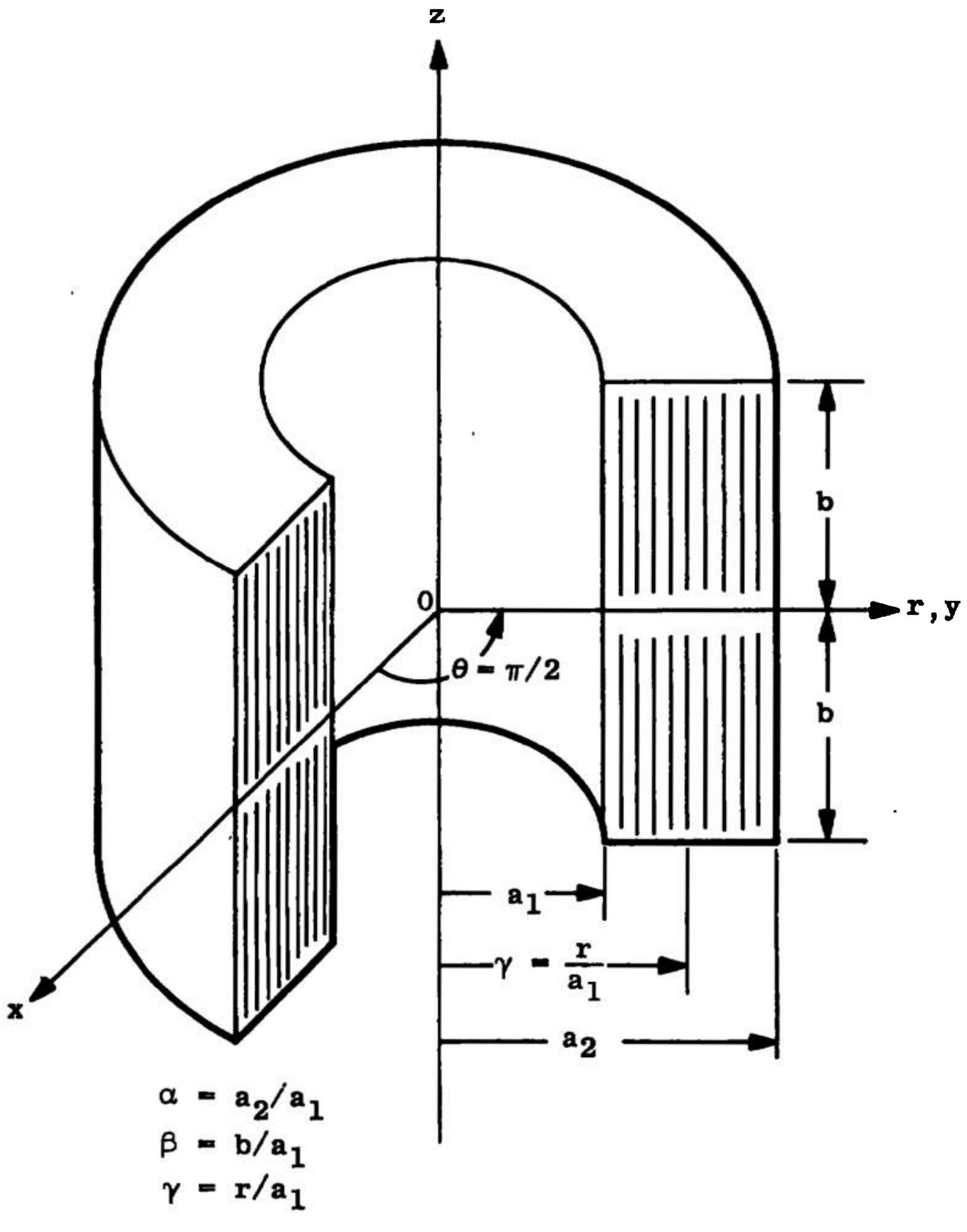

Figure 1. Cylindrical magnet coil geometry and coordinate system.

dimensions are expressed in terms of the nondimensional shape parameters: (1) α, the ratio of a_2 to a_1, (2) β, the ratio of b to a_1, and (3) γ, the ratio of an intermediate radius r to a_1.

II. LITERATURE REVIEW

In a recent work, Hord [1] presented a summary of several previous studies [2 through 5] of the stresses in various type magnet coils and developed formulae for the stresses in cylindrical strip-wound coils by use of three different analytical models. The three models Hord considered are (1) monolithic disc: this model assumes an isotropic, homogeneous cylindrical disc subjected to the magnetic body forces; (2) floating shell: this concept assumes each conductor turn to be a self-supporting and unrestrained thin wall cylinder: and (3) magnetic pressure: the stress is assumed that incurred by a thick wall cylinder subjected to internal pressure equal to the magnetic energy density.

For the homogeneous disc model. formulae were developed for the axial, radial, and circumferential stress components. The radial and circumferential stresses were derived for both the plane stress and plane strain conditions. The circumferential stress component only was formulated for the floating shell and thick wall cylinder models. The formulae are dependent on the magnetic induction $\vec{B}$ and are applicable only for elastic deformations of the conductor material. Symmetrical flux distribution and uniform current density were assumed. Hord's analysis shows that the axial component of stress is on the order of 20 per cent of the maximum circumferential stress. The radial stress component was considered negligible. On the basis of the mode of failure of one magnet constructed of a stack of strip-wound, epoxy-bound coils, Hord concluded that (1) the homogeneous disc model analyzed under the assumption of plane stress is applicable for tightly-wound, epoxy impregnated coils, and (2) the floating shell model best fits loosely wound unbonded coils.

Daniels [3] also dealt with stresses in a strip-wound coil. By treating the windings as a homogeneous anisotropic material, the insulating space between turns was accounted for. It was concluded that each turn is in equilibrium under its own body forces and that axial compression does not affect the magnitude of the radial and circumferential stress components. Daniels also considered the stability of coil windings against deformation and concluded that certain of the outside turns are intrinsically unstable due to negative body forces in that region and that in the absence of elastic restraining forces, the outer turns may collapse upon adjacent turns resulting in coil failure by radially unsymmetric distortion of the windings.

More recently, Gersdorf, et al. [7] treated plastic as well as elastic deformations in magnet coil windings. The anisotropic nature of the windings and the conditions of stress compatibility were considered. Results similar to those of Hord [1] were obtained for the elastic stresses. However, it was pointed out that a positive radial stress is not possible in loosely wound coils because it would separate the windings at a very low value. To account for this, the windings were divided into two parts. For the inner part the radial stress was assumed to be zero so that essentially the floating shell condition was realized. For the outer part of the windings, the solution for the circumferential stress was very close to Hord's plane stress solution.

According to Furth [6], the axial magnetic field of an air core solenoid behaves like a two-dimensional gas in that it exerts a radial pressure equal to the magnetic energy density. Furth treated long solid-bodied coils of helical or single turn construction in terms of a thick wall cylinder with this magnetic pressure applied to the inside wall surface. Equations for both the radial and circumferential stresses were formulated. For thick coils the maximum tensile stress was indicated to be equal to the magnetic pressure. It was implied that the maximum magnetic field H_m attainable with such a magnet is equal to $(2\sigma_m/\mu_o)^{1/2}$ where σ_m is the maximum permissible stress for the magnet material.

Ignatchenko and Karpenko [8] also have studied the problem of stresses in solid-bodied coils. Using the theory of maximum shear stresses in the thick wall cylinder model, they concluded that the maximum achievable field is $(\sigma_m/\mu_o)^{1/2}$.

Several of these theories and models were employed in an attempt to determine the maximum field attainable without damage to an existing large, pulse operated magnet used to generate the B-field for an experimental magnetohydrodynamic accelerator [10]. The magnet is constructed of two stacks of thin coil discs wound from flat rectangular magnet wire. Due to significant differences in the results obtained, this study was made in an attempt to establish the most accurate model for such a coil. Data obtained from a small experimental strip-wound coil instrumented with strain gages and pulsed from a capacitor bank energy storage system are compared with stresses calculated by use of the models. The International System of Units is employed throughout except for the measured and calculated stresses presented in Chapter IV. These are expressed in Engineering System Units.

CHAPTER II

BODY FORCE ANALYSIS

I. MAGNETIC FIELD DISTRIBUTIONS AND BODY FORCES

It is necessary to develop analytical expressions for the magnetic body forces which generate the stresses in magnet windings. Consider the force acting on a charge q moving with velocity $\vec{v}$ through a magnetic field $\vec{H}$. The total magnetic force acting on the charge is given by the Lorentz force [11] as

$$\vec{f} = q\vec{v} \times \vec{B} , \tag{1}$$

in which $\vec{B} = \mu\vec{H}$ is the magnetic induction. The total force δF on a small conducting volume δV in which the charges move essentially with velocity $\vec{v}$ and experience the induction $\vec{B}$ is given by

$$\delta\vec{F} \cong n\ \delta V\ q\ (\vec{v} \times \vec{B}) \tag{2}$$

or in the limit by

$$\frac{dF}{dV} \triangleq \lim_{\delta V \to 0} [nq(\vec{v} \times \vec{B})] = \vec{J} \times \vec{B} \tag{3}$$

where n is the density of the current-carrying charges and it is noted that $\vec{J} = nq\vec{v}$. Thus, in order to determine the magnetic body force at any point within the current conductors of a magnet, it is necessary only to know the local values of $\vec{B}$ and $\vec{J}$. In this study as for most investigations of this problem in the literature, steady-state current density and steady-state magnetic fields are assumed. That is, it is assumed that $|\vec{J}|$ is constant and that $\vec{B}$ is equal for all values of time to the steady-state value. The validity of these assumptions for a pulsed coil is discussed in the latter part of this chapter.

Brown and others [12] have computed and tabulated numerical values for the steady-state axial and radial components (B_z and B_r, respectively) for thick, finite-length solenoids carrying uniform current density. Values of B_z and B_r are expressed in terms of B_o, the flux density at the geometric center of the coil, and are tabulated as functions of α, β, and γ for integer values of α and β. Typical distributions of B_z/B_o and B_r/B_o along with a typical flux linkage are superimposed on a coil cross section in Figure 2. It is apparent that B_r induces axial forces on the current conductors and gives rise to axial compressive stresses σ_z. The radial forces induced by B_z give rise to radial and circumferential stresses which tend to burst the coil. Data from Brown's tabulations are plotted in Figures 3, 4, 5, and 6 and show the variations of B_z and B_r with coil geometry.

In a more recent work, Brown and Flax [13] have computed and tabulated numerical values of H_z and H_r for semi-infinite solenoids with zero inner radius. Each field component is expressed nondimensionally and tabulated as a function of nondimensional field-point coordinates. Axially symmetric, uniform, azimuthal, steady-state current density is assumed. By superposition of appropriate semi-infinite solenoids, local values of H_z and H_r and, subsequently, of B_z and B_r

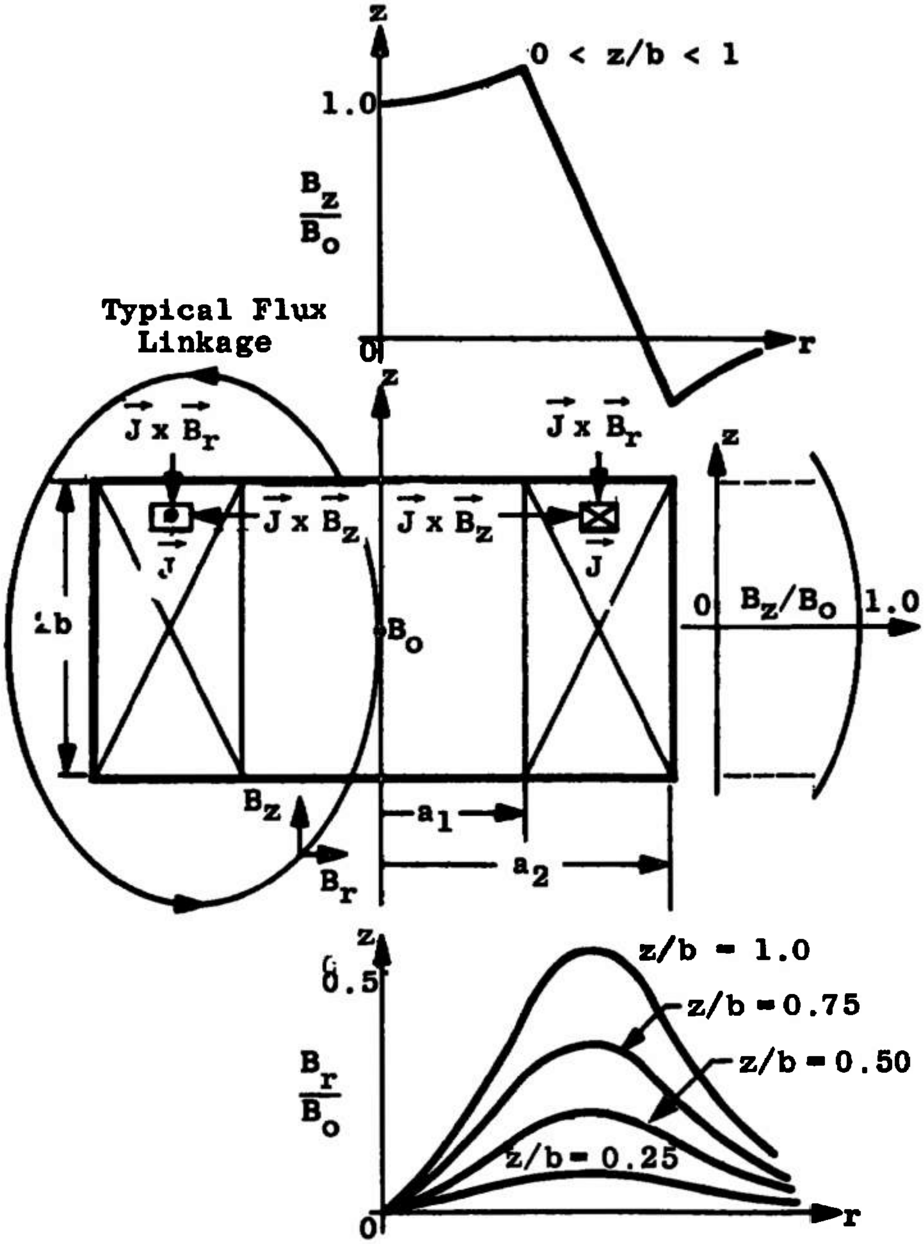

Figure 2. Plot of typical distributions of the axial and radial components of magnetic induction for a cylindrical coil carrying uniform current density.

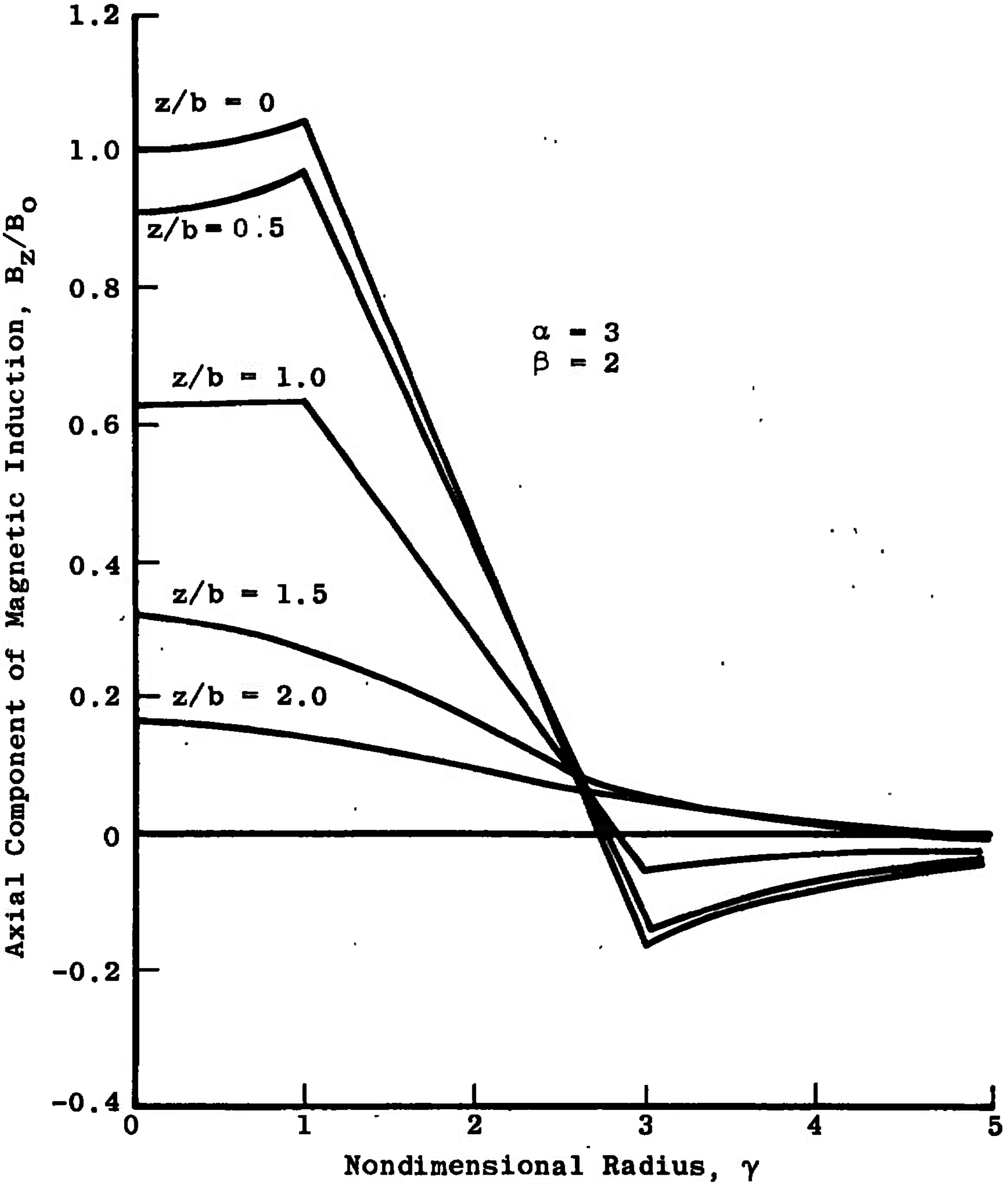

Figure 3. Plot of the axial component of magnetic induction for several axial positions in a cylindrical coil carrying uniform current density.

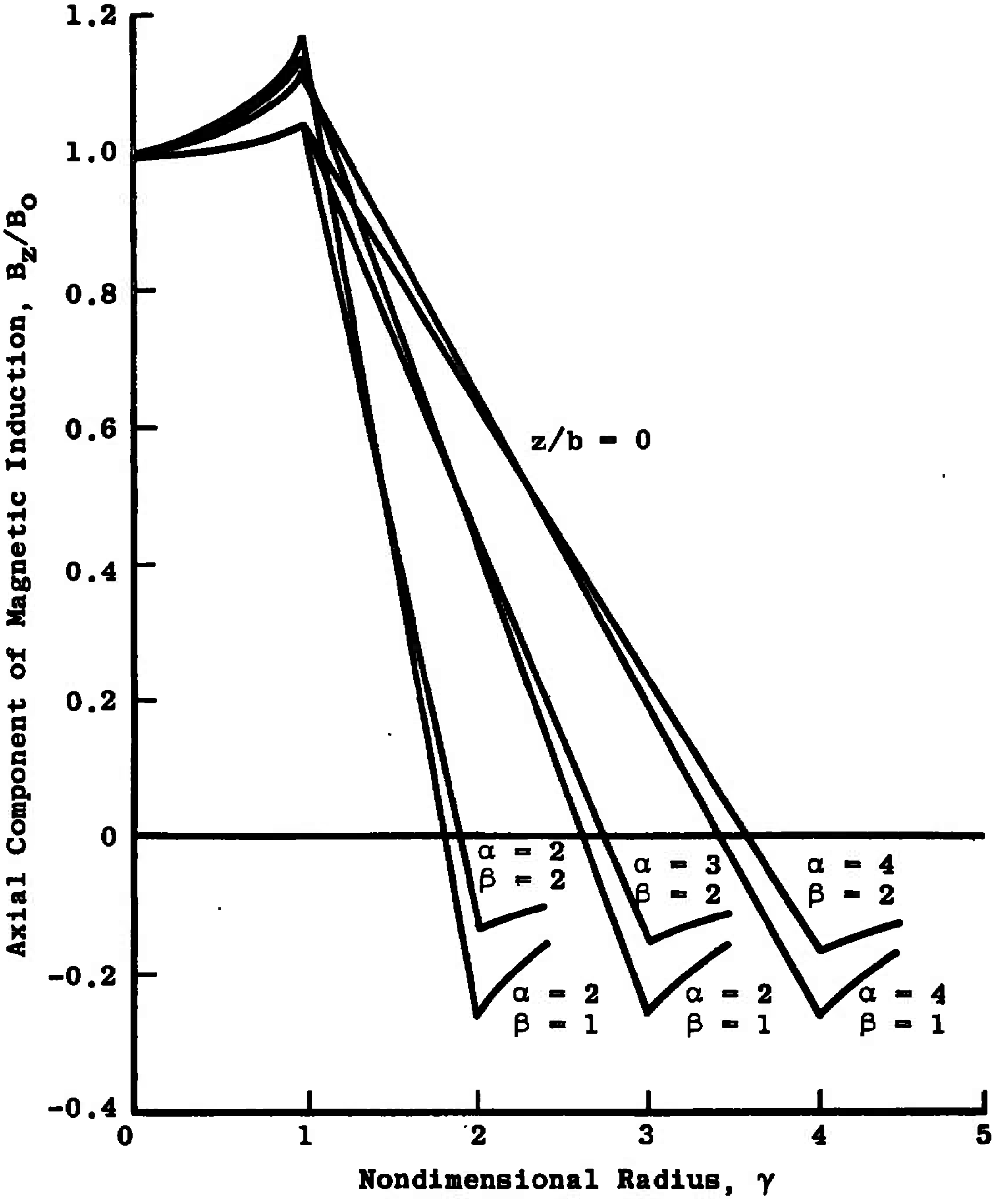

Figure 4. Plot of the axial component of magnetic induction for several values of α and β for a cylindrical coil carrying uniform current density.

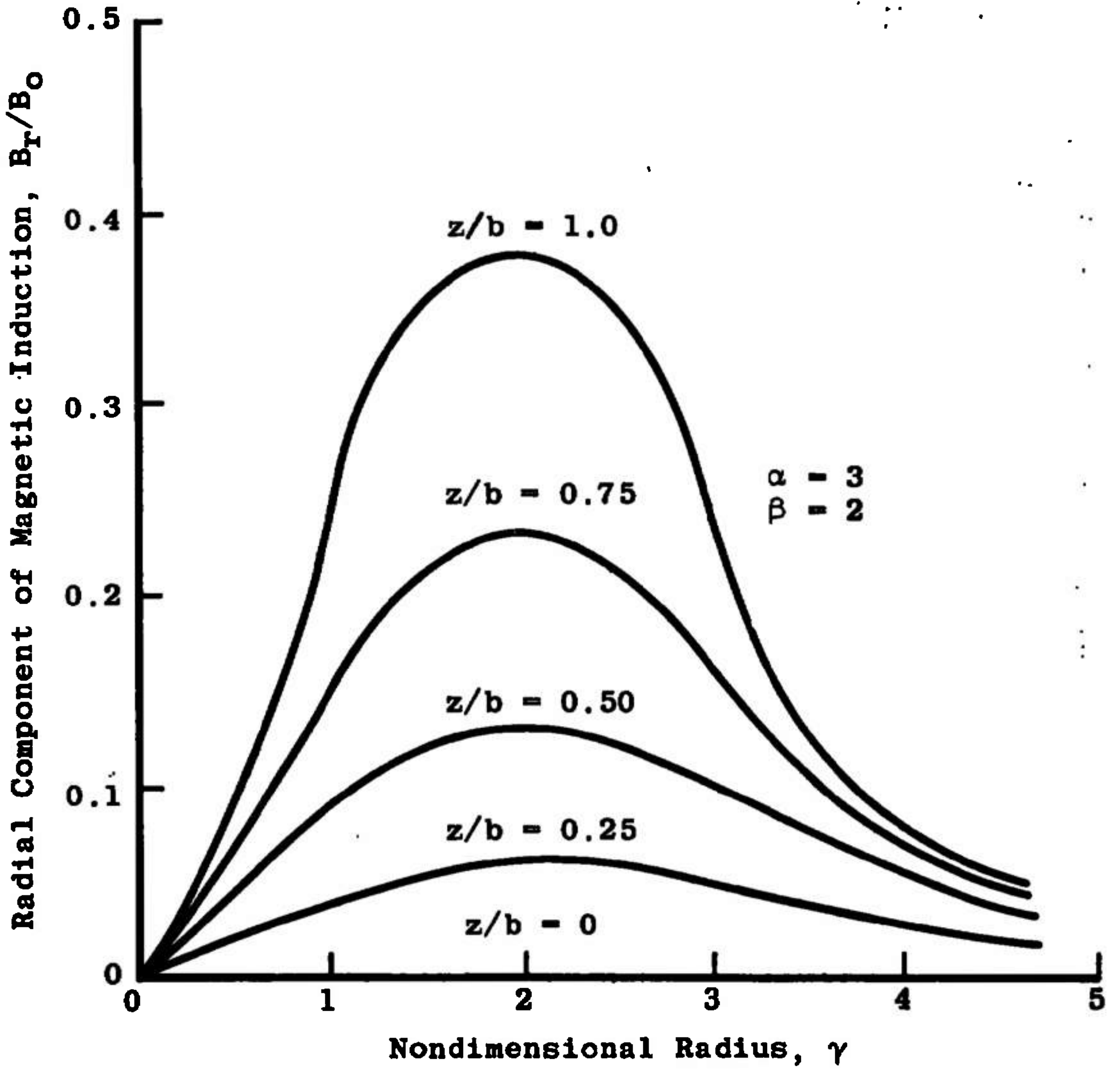

Figure 5. Plot of the radial component of magnetic induction for several axial positions in a cylindrical coil carrying uniform current density.

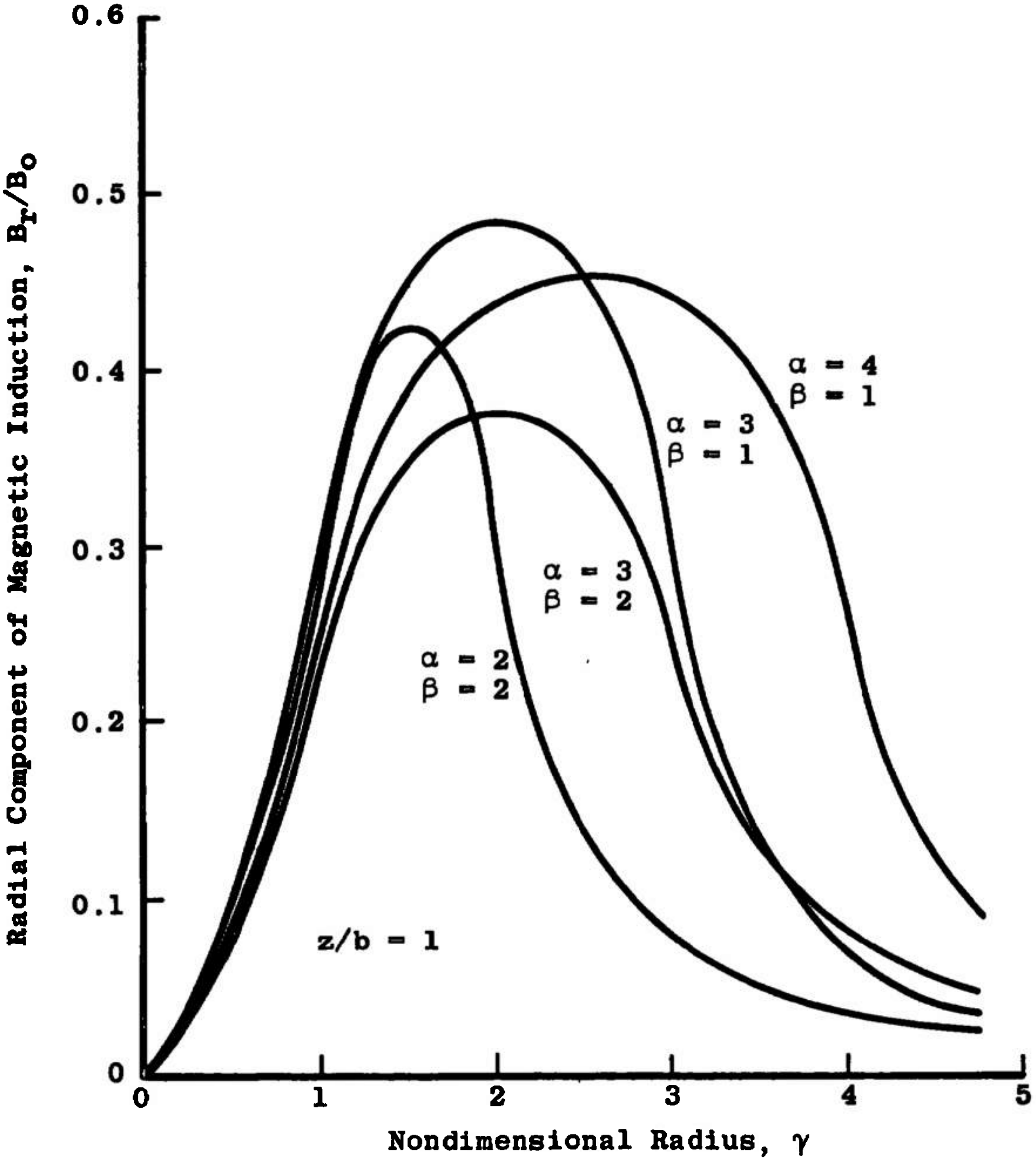

Figure 6. Plot of the maximum radial component of magnetic induction for several values of α and β for a cylindrical coil carrying uniform current density.

may be determined everywhere within any finite cylindrical coil carrying uniform current density. These tabulations facilitate the determination of field components in coils for which α and β are not integers and, thus, have been utilized in this study.

If the coil depicted in Figure 2, page 9, is wound with N turns and carries a uniform current of I amperes per turn, the current density at any point is

$$\vec{J} = \frac{NI}{2ba_1\lambda(\alpha-1)}\,\vec{e}_\theta \tag{4}$$

where the space factor λ is the ratio of the volume of current conductor to the total volume of the coil. In Appendix A it is shown that B_o can be expressed as

$$B_o = \frac{NI}{2b(\alpha-1)}\left(\frac{2\pi\beta}{5}\right)\ln\left[\frac{\alpha + (\alpha^2 + \beta^2)^{1/2}}{1 + (1 + \beta^2)^{1/2}}\right] \times 10^{-6}. \tag{5}$$

Equation (5) may be written as

$$B_o = \frac{10^{-6}\,NI}{2b(\alpha-1)}\,F(\alpha,\beta) \tag{6}$$

in which the term

$$F(\alpha,\beta) = \left(\frac{2\pi\beta}{5}\right)\ln\left[\frac{\alpha + (\alpha^2 + \beta^2)^{1/2}}{1 + (1 + \beta^2)^{1/2}}\right] \tag{7}$$

is called the field factor. Combination of Equations (3), (4), and (6) yields for any point within the conductor;

$$\frac{d\vec{F}}{dV} = \frac{10^6 B_o}{a_1 \lambda F(\alpha,\beta)} \left[\vec{e}_\theta \times (B_r \vec{e}_r + B_z \vec{e}_z)\right] \tag{8}$$

Thus, the radial force component is

$$\frac{d F_r}{dV} = \frac{10^6 B_z B_o}{a_1 \lambda F(\alpha,\beta)} \tag{9}$$

and the axial force component is

$$\frac{d F_z}{dV} = \frac{10^6 B_r B_o}{a_1 \lambda F(\alpha,\beta)} \tag{10}$$

As suggested by Hord [1] and as is apparent from Figure 3, page 10, in any plane perpendicular to the coil axis between z = -b and z = b, B_z within the coil windings ($1 \leq \gamma \leq \alpha$) may be expressed as

$$B_z = B_o [y + m (1-\gamma)], \tag{11}$$

where y is the value of B_z/B_o at $r = a_1$, and m is the absolute value of the slope of B_z/B_o. In Appendix B it is shown that an approximation for the distribution of B_r throughout the windings is

$$B_r = B_o \frac{z}{b} \left[m_1 + m_2 \sin\left(\frac{\gamma-1}{\alpha-1}\right)\pi\right] . \tag{12}$$

Thus, Equation (9) becomes

$$\frac{d F_r}{dV} = \frac{10^6 B_o^2}{a_1 \lambda F(\alpha,\beta)} [y + m (1-\gamma)] \tag{13}$$

and Equation (10) becomes

$$\frac{d\ F_z}{dV} = - \frac{10^6\ B_o^2}{a_1 \lambda\ F(\alpha,\beta)}\ \frac{z}{b}\left[m_1 + m_2 \sin\left(\frac{\gamma-1}{\alpha-1}\right)\pi\right] . \tag{14}$$

Equations (13) and (14) are used in Chapter III in the development of formulae for the magnet stresses.

II. COMMENTS ON THE STEADY-STATE ASSUMPTIONS

In formulating expressions for the stresses in magnet coils, uniform current density and steady-state magnetic fields usually are assumed. Thus, the validity of comparing theoretical stresses with those measured in a rapidly pulsed magnet coil must be questioned. Consider a cylindrical magnet coil spirally wound with several turns of wide strip conductor and energized by a half-sine pulse. The stresses which can be measured by use of electrical strain gages are those which exist on the surface of the conductors at various radial positions. For a pulsed coil the convenient reference point for data reduction purposes is the peak of the strain pulse. Thus, the points in question are: (1) does the magnetic field completely diffuse into the conductor and (2) does the current assume a uniform distribution during the pulse? For a multi-turn coil the two problems are related in some complex manner and to the knowledge of the writer an exact treatment has not been reported in the literature. Analysis of a simplified model will lend some insight to the problem.

Consider one turn of the cylindrical coil to be a thin cylindrical shell. If the radius of the cylinder is much greater than the wall thickness, the problem of diffusion of the magnetic field through the shell can be treated in terms of diffusion in a thin flat plate. Maxwell's equations for a linear isotropic conductor are:

$$\vec{\nabla} \times \vec{E} = -\frac{\partial \vec{B}}{\partial t} \tag{15}$$

$$\vec{\nabla} \times \vec{H} = \vec{J} + \frac{\partial \vec{D}}{\partial t} \tag{16}$$

$$\vec{\nabla} \cdot \vec{B} = 0 \tag{17}$$

$$\vec{\nabla} \cdot \vec{E} = 0 \ . \tag{18}$$

Other important relationships are:

$$\vec{B} = \mu \vec{H} \tag{19}$$

and, in the absence of material motion,

$$\vec{J} = \sigma \vec{E} \ , \tag{20}$$

where μ and σ are, respectively, the permeability and conductivity of the conductor. Substituting Equation (20) into Equation (15) yields

$$\frac{1}{\sigma} \vec{\nabla} \times \vec{J} = -\frac{\partial \vec{B}}{\partial t} \tag{21}$$

Also, substituting Equation (19) into Equation (16) and neglecting the displacement current term yields

$$\frac{1}{\mu} \vec{\nabla} \times \vec{B} = \vec{J} \ . \tag{22}$$

Now, taking the curl of Equation (22) and substituting into Equation (21) gives

$$\frac{1}{\mu\sigma} \vec{\nabla} \times (\vec{\nabla} \times \vec{B}) = - \frac{\partial \vec{B}}{\partial t} . \tag{23}$$

But, $\vec{\nabla} \times (\vec{\nabla} \times \vec{B}) = \vec{\nabla}(\vec{\nabla} \cdot \vec{B}) - \vec{\nabla}^2 \vec{B}$ and $\vec{\nabla} \cdot \vec{B} = 0$; thus, Equation (23) becomes

$$\frac{1}{\mu\sigma} \vec{\nabla}^2 \vec{B} = \frac{\partial \vec{B}}{\partial t} \tag{24}$$

which is the diffusion equation.

Equation (24) has been solved [11] for the diffusion of a one-dimensional magnetic field into a parallel conducting plate as indicated in Figure 7. The length and width of the plate were assumed to be large enough compared with the thickness d to consider the plate as infinitely large in the x- and y-directions.

For an applied step in $\vec{B}$ the solution for B_x was shown [11] to be

$$B_x = B \left[1 - \sum_{n \text{ odd}} \frac{4}{n\pi} \sin \frac{n\pi z}{d} e^{-\alpha_n t} \right] \tag{25}$$

where

$$\alpha_n = \frac{n^2 \pi^2}{\mu\sigma d^2} . \tag{26}$$

The time constant for the fundamental component (n=1) is defined as

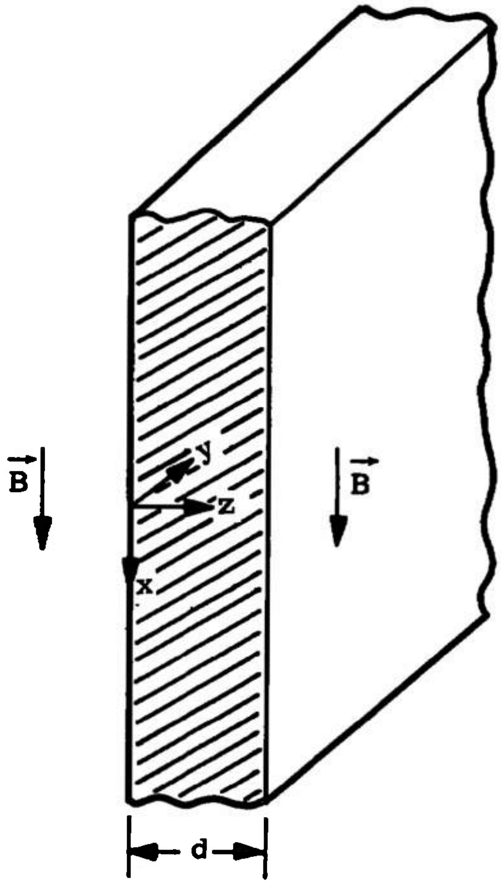

Figure 7. Transient magnetic field diffusion in a thin flat plate.

$$\tau = \frac{1}{\alpha_1} = \frac{\mu\sigma d^2}{\pi^2} . \tag{27}$$

The higher harmonics damp out much faster: therefore, the fundamental time constant is called the diffusion time constant. It can be shown [11] that after a time $t > 3\tau$, the field is almost completely diffused into the plate. For copper $\mu \cong \mu_0$, and $\sigma = 5.9 \times 10^7$ at 293°K: thus,

$$\tau = 7.52\ d^2 . \tag{28}$$

For the experimental magnet, $d = 8.1 \times 10^{-4}$ meters and τ is approximately 5×10^{-6} seconds.

As indicated above, the analogy between this thin plate model and a multi-turn, strip-wound coil is to let the cross section of the plate in the x-y plane represent the cross section of one conductor turn in the coil. The magnetic field then corresponds to the coil axial field. Obviously, the effects of the self axial field of the turn as well as the effects of radial fields generated by the other turns must also be considered.

Now consider the problem of transient current density distribution for the flat plate model. From Equation (16) it easily follows upon setting $\mu = \mu_0$ and neglecting displacement current that

$$\mathfrak{J}_y = \frac{1}{\mu_0} \frac{\partial B_x}{\partial z} = - \frac{B}{\mu_0 d} \sum_{n\ \mathrm{odd}} 4 \cos\left(\frac{n\pi z}{d}\right) e^{-n^2 t/\tau} . \tag{29}$$

Note that J_y is produced by the diffusing magnetic flux density and goes to zero as B_x reaches steady-state.

The diffusion problem for the real coil requires a more general solution of the diffusion equation. However, the numerical value of the diffusion time constant for the simplified model is assumed indicative of the time to reach steady-state. Thus, for variations in coil excitation whose characteristic times are much longer than τ, it is assumed that the steady-state values of $\vec{J}$ and $\vec{B}$ are applicable.

CHAPTER III

STRESS ANALYSIS

In theoretical analyses of the stress distributions within magnet coils, several analytical models have been assumed [1-9]. Three such models are [1]: (1) an isotropic, homogeneous cylindrical disc subjected to the magnetic body forces, (2) a floating shell concept which assumes each conductor to be a self-supporting and unrestrained thin wall cylinder, and (3) a thick wall cylinder subjected to internal pressure equal to the magnetic energy density. The derivations of the stress formulae developed by Hord [1] for these three models are outlined in this chapter.

I. MONOLITHIC DISC

Consider the stresses acting on an incremental volume element of a thin disc taken from a circular cylinder of constant wall thickness as depicted in Figure 8. Timoshenko [14] shows that if the cylinder has axisymmetric loading and the incremental element is subjected to a radial body force dF_r/dV as indicated in Figure 9, the equation of radial equilibrium is

$$\sigma_\theta - \sigma_r - r\frac{d\,\sigma_r}{dr} = r\frac{d\,F_r}{dV}\,. \qquad (30)$$

Plane Stress

For the case of plane stress, $\sigma_z = 0$; therefore σ_θ and σ_r may be written [15] in terms of radial displacement u as follows:

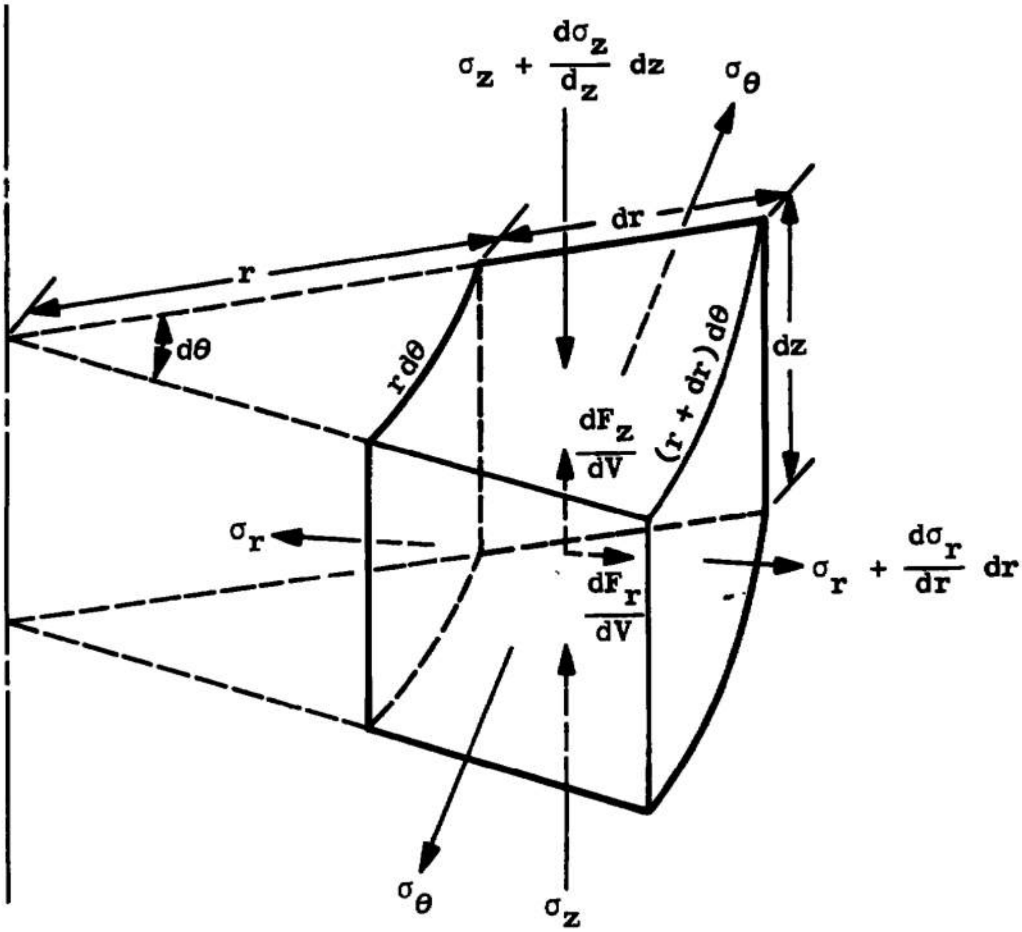

Figure 8. Equilibrium of an incremental volume element of a circular cylinder subjected to axisymmetric body forces.

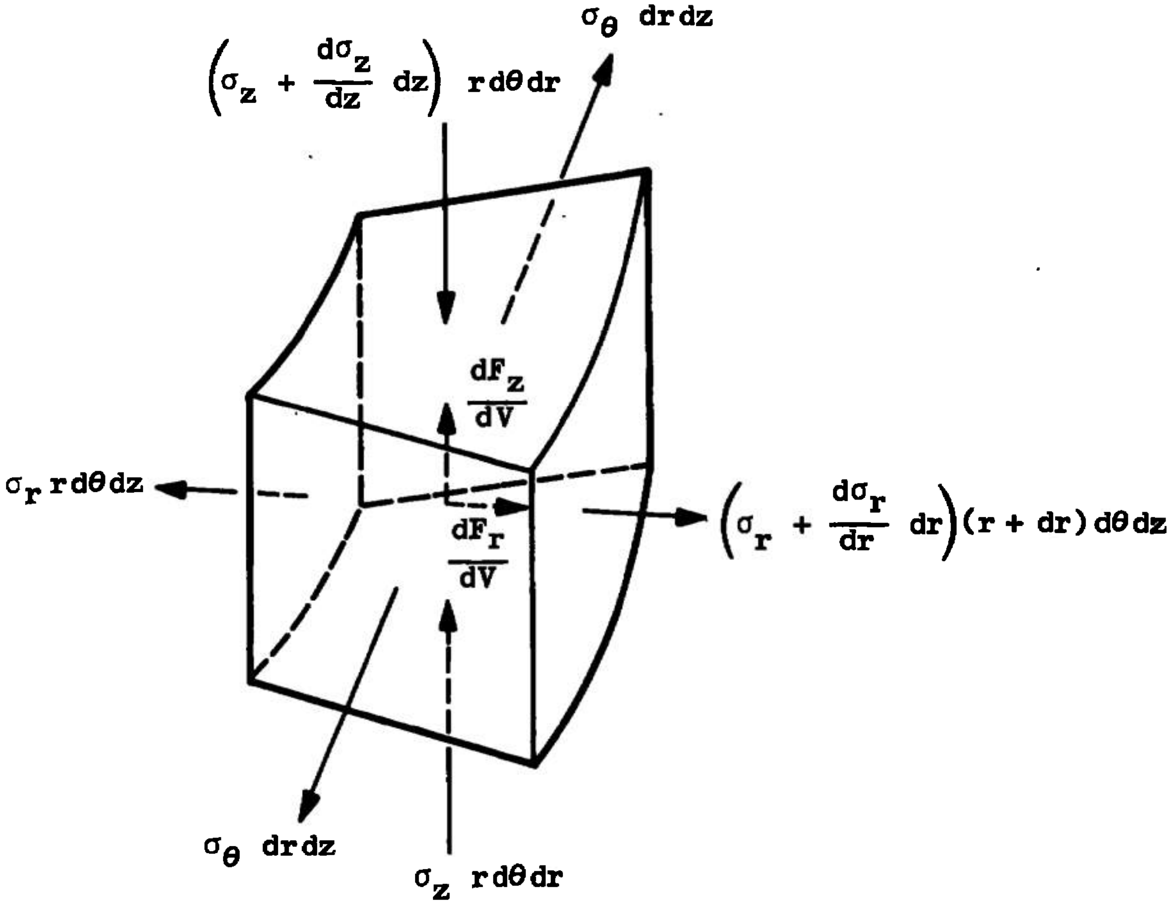

Figure 9. Forces acting on an incremental element of a circular cylinder subjected to axisymmetric body forces.

$$\sigma_\theta = \frac{E}{1 - \nu^2}\left[\frac{u}{r} + \nu \frac{du}{dr}\right] \tag{31a}$$

and,

$$\sigma_r = \frac{E}{1 - \nu^2}\left[\frac{du}{dr} + \nu \frac{u}{r}\right], \tag{31b}$$

where E is the modulus of elasticity and ν is Poisson's ratio. By combining Equations (13), (30), and (31) the equilibrium equation becomes

$$\frac{d^2u}{dr^2} + \frac{1}{r}\frac{du}{dr} - \frac{u}{r^2} = K[y + m\ (1-\gamma)], \tag{32}$$

where,

$$K = -\frac{10^6\ B_o{}^2\ (1 - \nu^2)}{a_1 \lambda\ E\ F(\alpha,\beta)} .$$

Equation (32) has the general solution

$$u = C_1 r + \frac{C_2}{r} + Kr^2\left[\frac{y+m}{3} - \frac{mr}{8a_1}\right]. \tag{33}$$

The constants C_1 and C_2 may be determined by combining Equations (31b) and (33) and applying the boundary conditions $\sigma_r = 0$ at $r = a_1$ and $r = a_2$; thus,

$$C_1 = -\frac{K\ Q_1\ a_1}{24} , \tag{34a}$$

and,

$$C_2 = -\frac{K\ Q_2\ a_1{}^3}{24} , \tag{34b}$$

where $Q_1 \equiv \frac{1}{1+\nu}\{Q_2(1-\nu) + 8y(2+\nu) + m(7+5\nu)\}$ and,

$$Q_2 \equiv - \frac{1}{1-\nu} \left(\frac{\alpha^2}{\alpha^2-1}\right)\{8y(2+\nu)(1-\alpha)+m\ [(7+5\nu) - 8\alpha(2+\nu) + \alpha^2\ (9+3\nu)]\} \ .$$

Now, by substituting Equations (33) and (34) into Equations (31) the circumferential and radial stress distributions for the condition of plane stress may be written as

$$\sigma_\theta = \frac{10^6\ B_o^2}{24\lambda\ F(\alpha,\beta)} \left[Q_1(1+\nu)+Q_2(1-\nu)\ \frac{1}{\gamma 2} + 3m(1+3\nu)\gamma^2-8(1+2\nu)(y+m)\gamma\right] \quad (35)^1$$

$$\sigma_r = \frac{10^6\ B_o^2}{24\lambda\ F(\alpha,\beta)} \left[Q_1(1+\nu)-Q_2(1-\nu)\ \frac{1}{\gamma^2} + 3m(3+\nu)\gamma^2-8(2+\nu)(y+m)\gamma\right]. \quad (36)$$

Plane Strain

For the case of plane strain the axial strain ε_z is assumed to be zero. For this case σ_θ and σ_r in terms of displacement are written as [16]:

$$\sigma_\theta = \frac{E}{(1+\nu)(1-2\nu)} \left[(1-\nu)\ \frac{u}{r} + \nu\ \frac{du}{dr}\right] \quad (37a)$$

and,

---

[1] The stresses are in newtons/meter^2 when B_o is expressed in webers/meter^2. To convert to psi multiply B_o^2 by 145 x 10^{-6}.

$$\sigma_r = \frac{E}{(1+\nu)(1-2\nu)}\left[(1-\nu)\frac{du}{dr} + \nu\frac{u}{r}\right] \qquad (37b)$$

By substituting Equations (37) into Equation (30) the equilibrium equation in terms of displacement is obtained. After solving for u and substituting back into Equations (37) the circumferential and radial stresses for plane strain are written as

$$\sigma_\theta^* = \frac{10^6\,B_o^2}{24\lambda\,(\nu-1)F(\alpha,\beta)}\left[Q_1^* - Q_2^*\,\frac{(1-2\nu)}{\gamma^2} + 8\gamma(\gamma+m)(1+\nu) - 3m\gamma^2(1+2\nu)\right] \qquad (38)$$

$$\sigma_r^* = \frac{10^6\,B_o^2}{24\lambda\,(\nu-1)F(\alpha,\beta)}\left[Q_1^* - Q_2^*\,\frac{(2\nu-1)}{\gamma^2} + 8\gamma(\gamma+m)(2-\nu) - 3m\gamma^2(3-2\nu)\right], \qquad (39)$$

where

$$Q_1^* = -8\gamma(2-\nu)\left(\frac{\alpha^2}{\alpha+1} + 1\right) + m(7-2\nu)\left(\frac{1}{\alpha^2-1}\right) - \frac{m\alpha^2}{\alpha^2-1}\left[8\alpha\,(2-\nu) + 3\alpha^2(2\nu-3)\right],$$

and

$$Q_2^* = \frac{\alpha^2}{(\alpha^2-1)(2\nu-1)}\left\{8\gamma(2-\nu)(1-\alpha)+m\,[(7-2\nu) - 8\alpha(2-\nu) - 3\alpha^2(2\nu-3)]\right\}.$$

Axial Compression

Now consider the case of axial compression in the monolithic disc. Axial equilibrium of the incremental element shown in Figure 9, page 24, requires

$$\frac{d\sigma_z}{dz} = \frac{dF_z}{dV} . \tag{40}$$

Combining Equations (14) and (40) yields

$$\frac{d\sigma_z}{dz} = \frac{10^6 B_o^2}{a_1 \lambda F(\alpha,\beta)} \frac{z}{b}\left[m_1 + m_2 \sin\left(\frac{\gamma-1}{\alpha-1}\right)\pi\right] \tag{41}$$

After integration of Equation (41) and invoking the boundary condition $\sigma_z = 0$ at $z = b$, the axial stress distribution within any plane perpendicular to the axis of the coil is given by

$$\sigma_z = -\frac{10^6 B_o^2 (b^2-z^2)}{2b\, a_1 \lambda F(\alpha,\beta)}\left[m_1 + m_2 \sin\left(\frac{\gamma-1}{\alpha-1}\right)\pi\right] . \tag{42}$$

II. FLOATING SHELL METHOD

The so-called floating shell concept [1] yields a very simple solution for the circumferential stress component. Consider a strip-wound coil in which each turn is assumed to be a self-supporting and unrestrained thin-walled cylinder as depicted in Figure 10. The radial force dF_r on the element of circumference subtended by the angle $d\theta$ acts at an angle θ to the horizontal, and consequently its vertical component is $dF_r \sin\theta$. Thus equilibrium is satisfied by

$$2\,\sigma_\theta\, dr\, dz = \int_V dF_r \sin\theta . \tag{43}$$

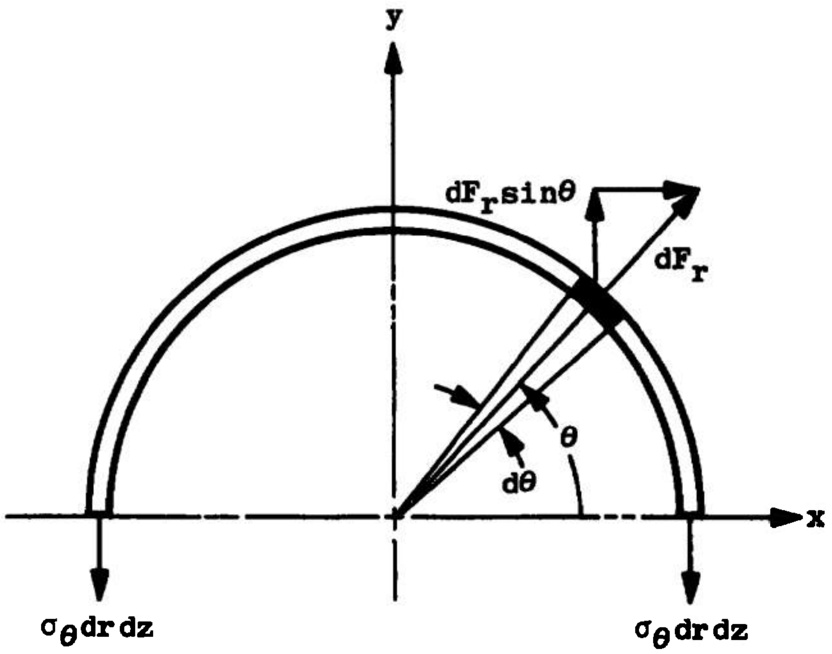

Figure 10. Equilibrium of a differential length of a thin walled cylinder subjected to axisymmetric radial body forces.

But from Equation (13),

$$dF_r = \frac{10^6 B_o^2}{a_1 \lambda F(\alpha,\beta)} [y+m (1-\gamma)]dV \qquad (44)$$

and in cylindrical coordinates dV = r dr dθ dz. Regarding dr and dz as increments rather than differentials, Equation (44) becomes

$$\sigma_\theta = \frac{10^6 B_o^2}{2a_1 \lambda F(\alpha,\beta)} \int [y+m (1-\gamma)]r \sin \theta \, d\theta. \qquad (45)$$

Integration between the limits of 0 and π yields for the circumferential stress

$$\sigma_\theta = \frac{10^6 B_o^2}{\lambda F(\alpha,\beta)} \gamma[y+m(1-\gamma)]. \qquad (46)$$

III. MAGNETIC PRESSURE CONCEPT

Since the dimensions of $|\vec{B}|^2/2\mu$ are those of energy density, and therefore of pressure, the magnetic forces may be interpreted as resulting from differences in magnetic pressure. If the magnetic pressure concept is applied to incremental elements in the conductor volume, it may be shown that body forces result which are identical with the $\vec{J} \times \vec{B}$ interpretation.

An approximate approach [1,5,6] treats the magnet coil as a thick walled pressure vessel subjected to an internal magnetic pressure P_m concentrated at the inside wall, where

$$P_m = \frac{B^2}{2\mu_o}\bigg|_{\substack{z/b=0\\ \gamma=1}} \quad . \tag{47}$$

This neglects the pressure exerted at the outer radius of the coil and, it is to be noted for the coil geometries considered here that

$$B\bigg|_{\substack{z/b=0\\ \gamma=1}} > B_o \tag{48}$$

as evident from Figure 4, page 11. In the literature B in Equation (47) is taken as B_o which is only true for an infinite solenoid, or "scaling factors" are induced to account for the larger induction at $\gamma = 1$ for finite coils [17]. Pursuing a method similar to that used in deriving the plane stress formulae, the circumferential stress for a thick-walled cylinder subjected to internal pressure P_m is found to be

$$\sigma_\theta = \frac{a_1^2 P_m}{a_2^2 - a_1^2}\left(1 + \frac{a_2^2}{r^2}\right) \tag{49}$$

Rearranging Equation (49) yields the form

$$\sigma_\theta = \frac{B^2\Big|_{\substack{z/b=0\\ \gamma=1}}}{2\mu_o(\alpha^2 - 1)}\left[1 + \left(\frac{\alpha}{\gamma}\right)^2\right] . \tag{50}$$

CHAPTER IV

EXPERIMENTAL RESULTS

Several experiments were conducted with a cylindrical strip-wound magnet in order to determine the variation of the circumferential stress with radial position at the coil midplane. The magnet was energized by a half-sine current pulse from a 30,000 microfarad energy storage capacitor bank. During each experiment, simultaneous measurements were made of B_o and the circumferential strain ϵ_θ at one of several positions within the coil winding.

I. MAGNET DESCRIPTION

The experimental magnet was constructed of electrolytic tough pitch copper strip conductor wound with alternate layers of mylar film insulation onto a hollow nylon cylinder. Prior to winding the copper conductor was vacuum annealed to a dead soft condition. Yield strength and Young's modulus of the annealed copper were experimentally determined to be 7000 psi and 15 × 10^6 psi, respectively. Poisson's ratio for copper is 0.355. Physical characteristics of the coil are given in Table I. During winding a resistance-type strain gage was bonded to the conductor on approximately every fourth turn. Each gage was oriented to sense the circumferential strain component at the coil midplane. This particular coil configuration was arrived at by considering (1) the magnitude of strain which could be induced with the

TABLE I

PHYSICAL CHARACTERISTICS OF THE EXPERIMENTAL MAGNET COIL

Conductor Thickness	(meters x 10^{-2})	.081
Number of Turns	N	46.7
Inductance	L (hys x 10^{-6})	101
Resistance	R (ohms x 10^{-3})	6.8
Coil Half-Length	b (meters x 10^{-2})	1.91
Coil Inside Radius	a_1 (meters x 10^{-2})	1.91
Coil Outside Radius	a_2 (meters x 10^{-2})	6.10
Radial Shape Parameter	α (a_2/a_1)	3.2
Axial Shape Parameter	β (b/a_1)	1.0
Space Factor	λ	0.90

available energy supply, (2) the maximum voltage which could be applied without danger of breakdown of the strain gage insulation, and (3) the necessity of a fairly uniform magnetic field over the axial space occupied by the strain gages to minimize errors in the strain measurements.

Theoretical values for the axial and radial components of magnetic induction for the coil as determined from the tabulations of Brown and Flax [13] are plotted in Figures 11 and 12. From Figure 11 the values of y and $|m|$ in Equation 11 are found to be 1.134 and 0.634, respectively. Points from the curves in Figure 12 are used in Appendix B for calculations of m_1 and m_2 in Equation (12).

II. ENERGY SUPPLY

The magnet energy supply consisted of a bank of 950 oil-filled 125 μf energy storage capacitors with a charging system and switching circuit to deliver the energy to the magnet. The capacitors were connected in a series-parallel arrangement to yield an equivalent capacitance C of approximately 30,000 μf. A schematic diagram of the system is shown in Figure 13. The switching ignitron was a National Electronics, Incorporated Model NL-1037. The ignitron was fired by a 1 kv pulse from a high voltage supply one millisecond after initiation of the data recording instruments. During the experiments the capacitor charge voltage V_o was limited to 500 volts to prevent possible breakdown of the strain gage insulation and subsequent damage to measuring instruments. Five hundred volts was not sufficient to maintain

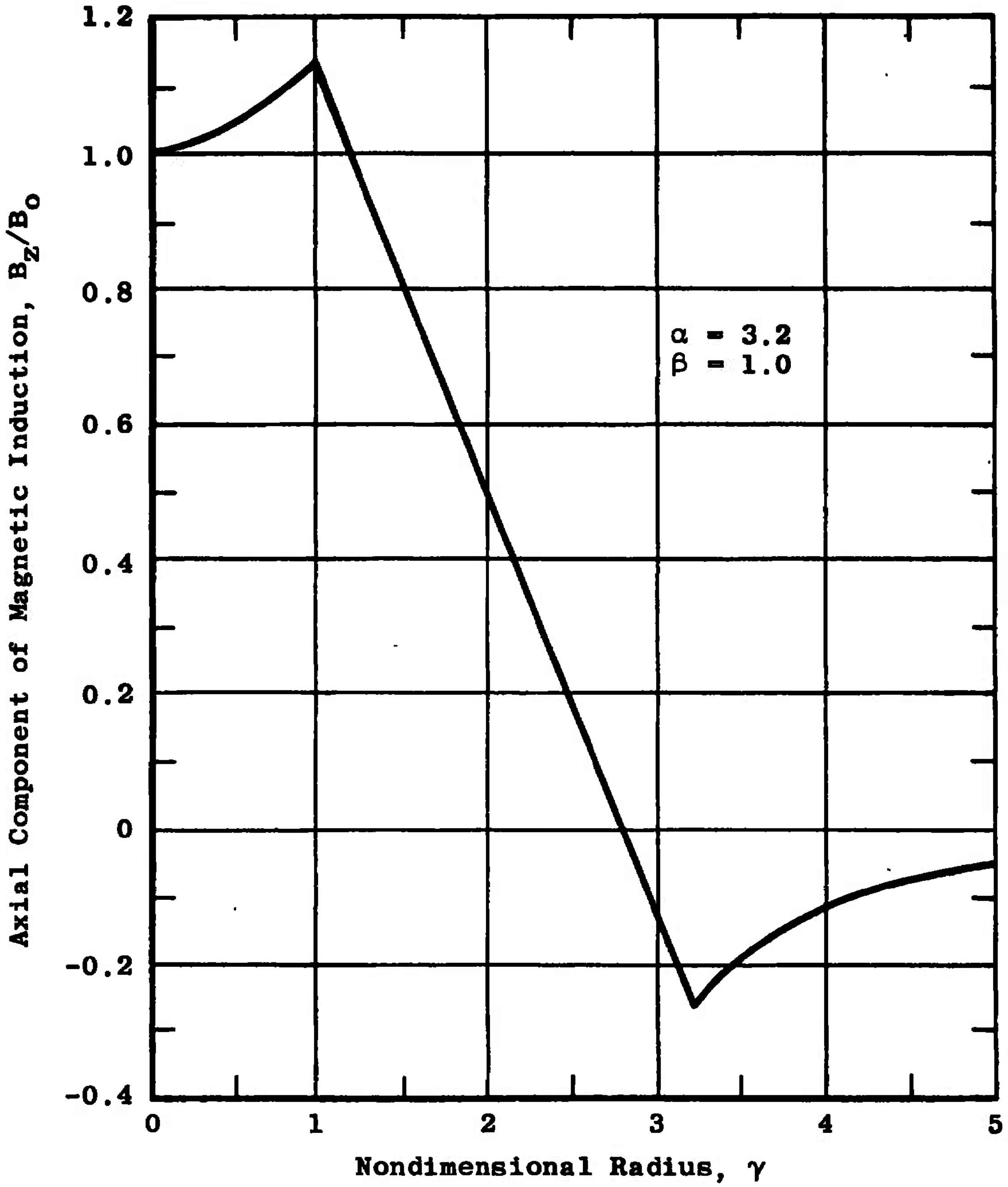

Figure 11. Plot of the axial component of magnetic induction at the midplane of the experimental coil.

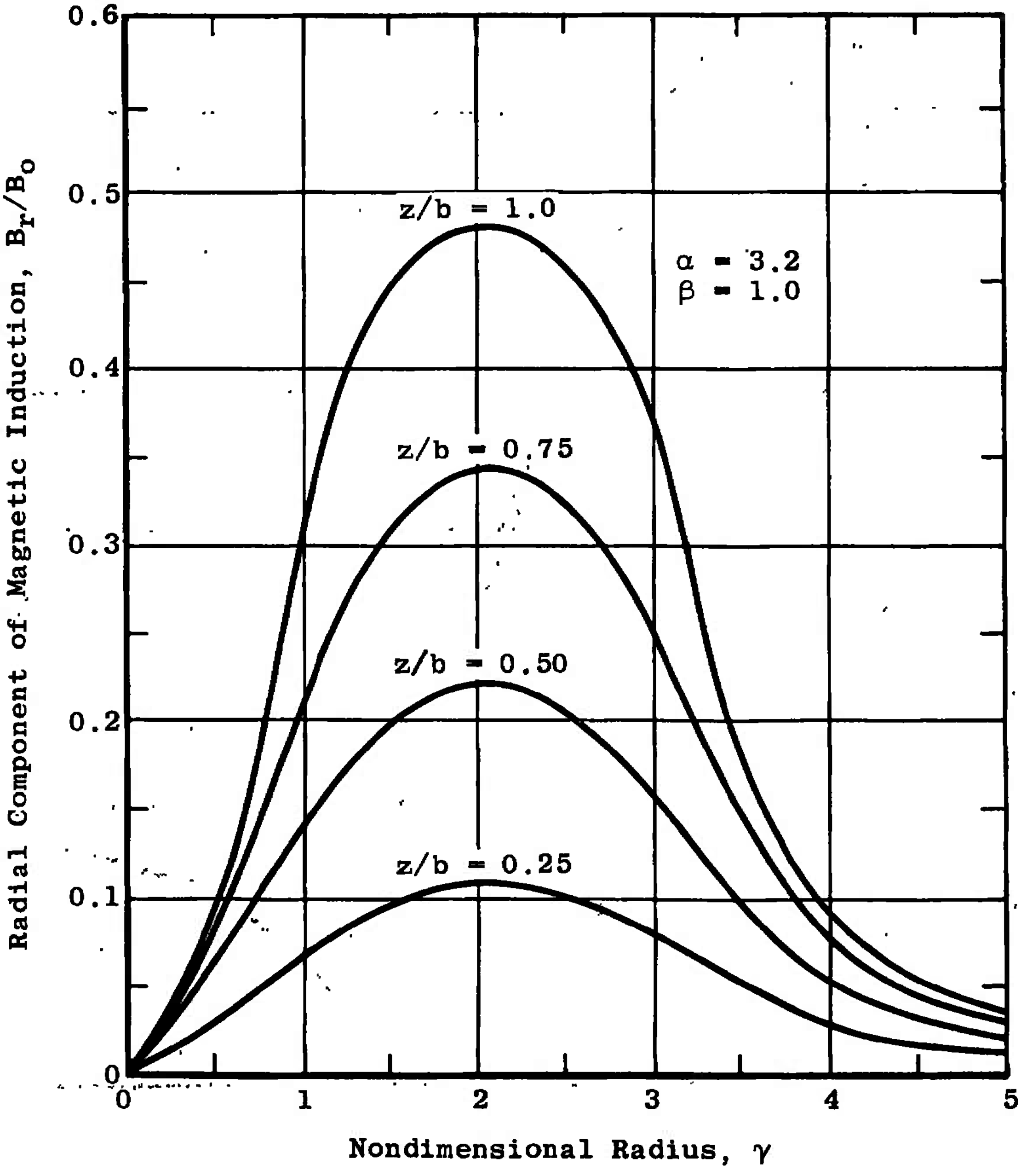

Figure 12. Plot of the radial component of magnetic induction for several axial positions in the experimental coil.

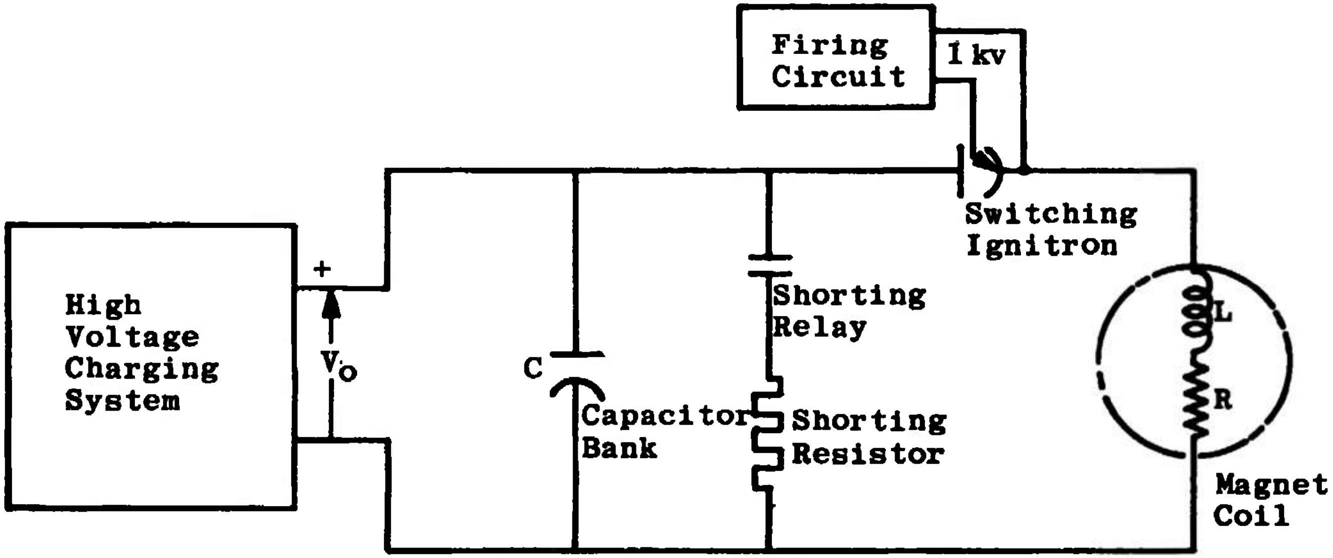

Figure 13. Schematic diagram of the magnet energy supply system.

ionization of the ignitron; therefore, the circuit was interrupted at zero current and the resulting magnet current was a half-sine pulse. Resistance of the coil is negligible; thus, peak value of the current was $V_o\ (C/L)^{1/2}$ (approximately 8000 amperes for V_o = 500 volts) and the pulse width was $\pi(LC)^{1/2}$ (approximately 5.8 milliseconds). The high voltage relay and shorting resistor indicated in Figure 13 were used to remove residual charge from the capacitors after each "shot".

III. INSTRUMENTATION

Measurement of strain in the magnet conductors was accomplished with a carrier amplifier system used to excite and measure the output of a strain gage bridge. Magnetic induction was measured by integrating the voltage output of a search coil positioned at the geometric center of the magnet. This integrated signal then was displayed simultaneously with the strain signal on a dual beam oscilloscope. A camera was used to obtain permanent records of the oscilloscope traces. Additional equipment included an active low pass filter to eliminate high frequency noise generated by the carrier system and a delay network for synchronization of the oscilloscope trigger with firing of the ignitron. A block diagram of the system is shown in Figure 14. A more thorough description of the instrumentation is given in Appendix C.

IV. DATA

The raw data obtained consist of a series of photographs of oscilloscope traces of the strain and magnetic induction signals. A

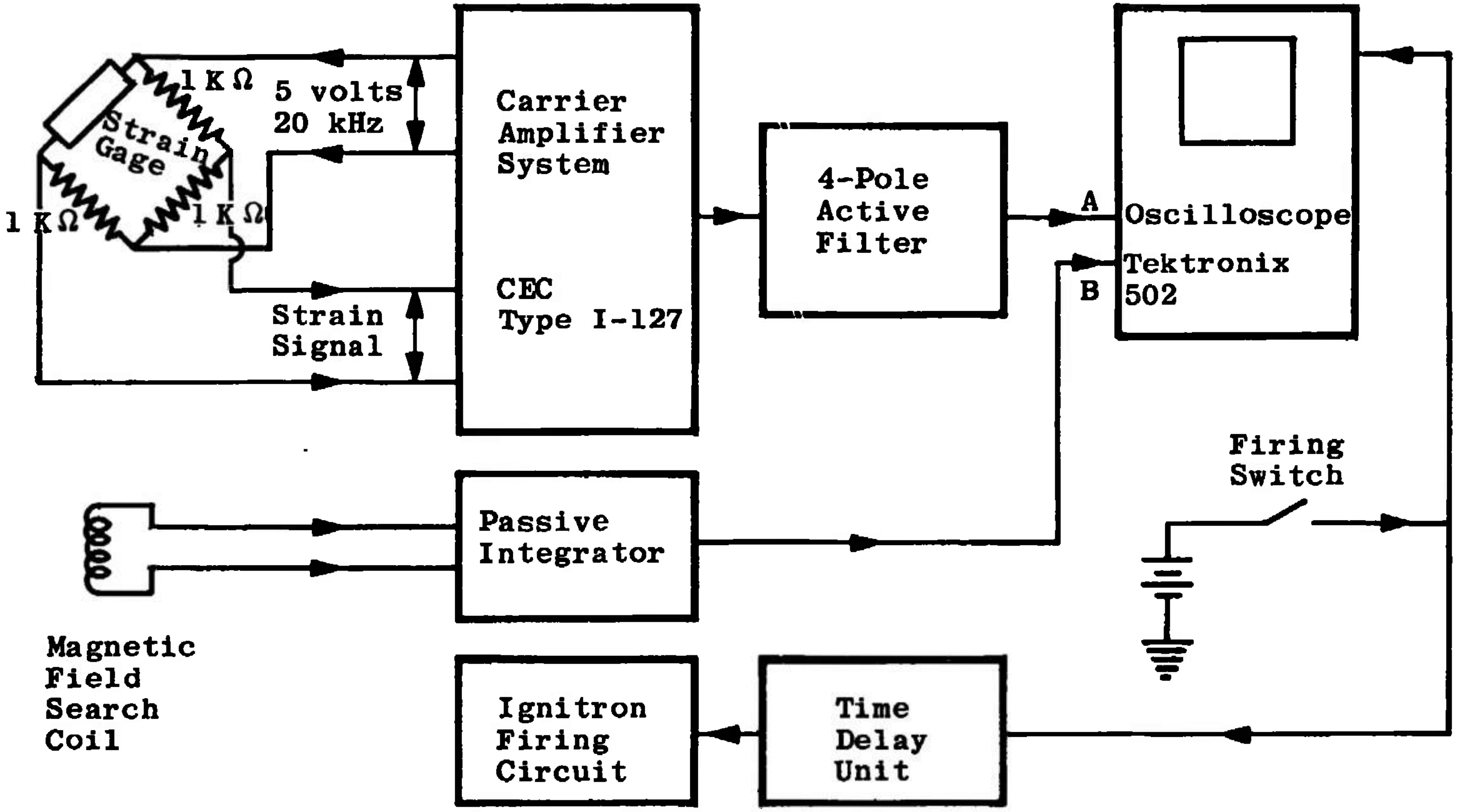

Figure 14. Block diagram of the magnet instrumentation system.

typical oscilloscope trace of the signals is shown in Figure 15. The top trace is the strain signal. By use of the appropriate calibration factors the peak values of the oscillograph deflections are converted to circumferential strain ε_θ and magnetic induction B_o. The stress then is computed by use of the relation $\sigma_\theta = \varepsilon_\theta E$. The stress may be expressed in a rationalized form by dividing σ_θ by B_o^2. The measured values of ε_θ for several radial positions at the coil midplane along with corresponding values of σ_θ, B_o, and σ_θ/B_o^2 are presented in Table II. In Figure 16, experimental values of σ_θ/B_o^2 are plotted versus the nondimensional radius γ to show the variation of σ_θ across the radial dimension of the magnet winding. Also plotted in Figure 16 are Equations (35), (36), (38), (39), (42), (46), and (50) as evaluated for the test magnet configuration.

V. DISCUSSION

As can be seen from Figure 16 the experimentally determined stress distribution does not agree closely with any of those computed by use of analytical models. However, Equation (46) developed from the floating shell concept predicts a distribution which has the same general shape as the experimental distribution. The experimental values of σ_θ are less than floating shell theory near the inside radius and are maximum at a greater radial position than the calculated maximum. Of particular interest is the fact that a compressive circumferential stress as predicted by Equation (46) was measured near the outside radius. As indicated by the curves for Equations (35) and (38),

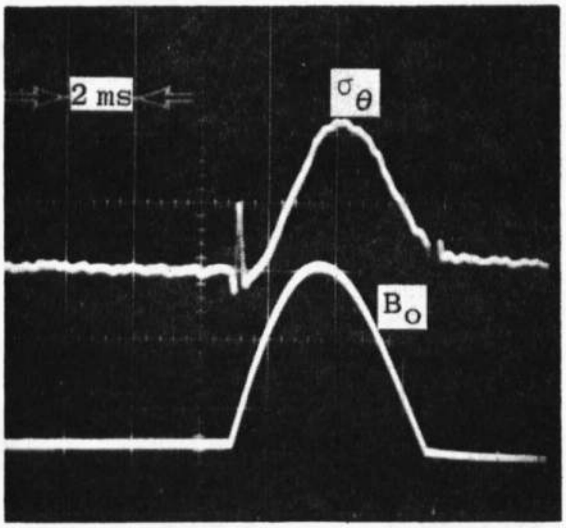

Figure 15. Oscillograph record of typical strain and induction signals.

TABLE II

TABULATED VALUES OF ε_θ, σ_θ, B_o, AND σ_θ/B_o^2 FOR THE EXPERIMENTAL MAGNET COIL

Nondimensional Radius, γ	ε_θ (micro-inches/inch)	σ_θ (psi)	B_o (webers/meter^2)	σ_θ/B_o^2 (psi[weber/meter^2]^2)
1.04	31.6	474	2.91	56
	59.0	885	3.06	95
	68.1	1020	3.38	89
1.26	63.6	954	3.05	103
	90.8	1360	3.26	128
	97.3	1460	3.26	137
	84.2	1260	3.03	137
1.45	76.0	1140	2.87	138
	84.2	1260	3.01	139
	63.1	947	2.56	144
	84.2	1260	2.85	155
1.62	121.0	1820	3.26	171
	105.0	1580	3.03	172
	136.0	2040	3.44	172
	104.0	1560	2.96	178
1.91	121.0	1820	3.50	149
	90.8	1360	2.96	155
	132.0	1980	3.44	167

TABLE II (continued)

Nondimensional Radius, γ	ϵ_θ (micro-inches/inch)	σ_θ (psi)	B_o (webers/meter^2)	σ_θ/B_o^2 (psi[weber/meter^2]^2)
2.06	105.0	1580	2.97	179
	111.0	1670	2.97	189
	150.0	2250	3.44	190
	84.2	1260	2.56	192
2.29	109.0	1640	3.08	173
	124.0	1860	3.26	175
	109.0	1640	3.03	179
	113.0	1700	3.03	185
2.46	60.5	908	3.03	99
	34.2	513	2.21	105
	63.6	954	2.91	113
	68.1	1020	2.94	118
2.67	45.4	681	3.44	58
	42.1	632	3.03	69
	45.4	681	2.98	77
	26.3	395	2.21	81
2.83	13.6	204	2.89	25
	27.2	408	3.38	36
	22.7	341	3.03	37
	21.0	315	2.85	39

TABLE II (continued)

Nondimensional Radius, γ	ε_θ (micro-inches/inch)	σ_θ (psi)	B_o (webers/meter^2)	σ_θ/B_o^2 (psi[weber/meter^2]^2)
3.06	-34.1	-512	3.03	-56
	-36.3	-545	2.91	-64
	-21.0	-315	2.10	-71
	-43.1	-647	2.96	-74

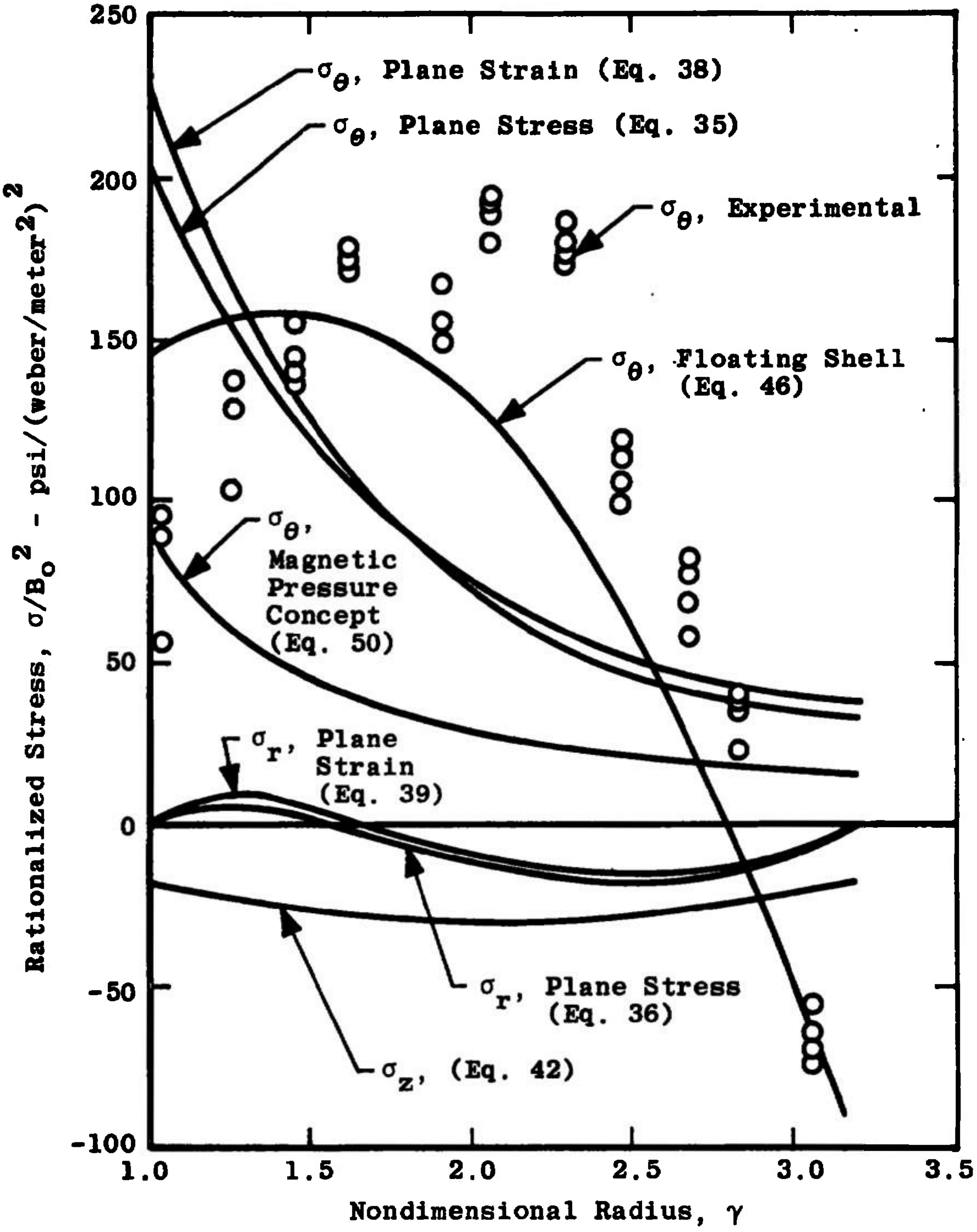

Figure 16. Plot of the theoretical and experimental stress distributions at the midplane of the experimental coil.

the plane stress and plane strain theories predict maximum circumferential stresses greater than either the measured stress or floating shell theory. Stresses calculated by use of the magnetic pressure method (Equation 50) are lower than those indicated by all other methods. Although no experimental values of the radial and axial stresses were obtained, Equations (36), (39), and (42) are plotted in Figure 16 to indicate the relative magnitude of these components as compared to the circumferential component. It is clearly seen that the circumferential stress is predominant.

Since the stresses plotted in Figure 16 are in terms of B_o^2, from a plot such as this for a particular coil, the nominal maximum field attainable without yielding can be determined for a given conductor. In Table III the conductor yield strength and maximum B_o are tabulated for several conductor materials. The tabulated values of maximum B_o are based on $\sigma/B_o^2 = 200$. Although a B_o of approximately 15 webers/meter^2 is indicated for the hard copper and copper alloys, strip-wound coils generally are limited to approximately 10 webers/meter^2 because of insulation fatigue problems.

TABLE III

MAXIMUM B_o ATTAINABLE WITH EXPERIMENTAL COIL GEOMETRY FOR SEVERAL CONDUCTOR MATERIALS

Conductor Material	Nominal Yield Stress (psi)	Maximum B_o (webers/meter^2)
Aluminum (annealed)	4,000	4.5
Copper (annealed)	8,000	6.3
Zirconium-Copper (annealed)	12,000	7.7
Beryllium-Copper No. 10 (annealed)	25,000	11.2
Copper (Hard)	40,000	14.1
Zirconium-Copper (hard)	50,000	15.8

CHAPTER V

CONCLUSIONS

From this study it must be concluded that of the analytical models investigated, the floating shell concept most nearly predicts the circumferential stress distribution in coils loosely wound with strip conductor. The plane stress theory for a monolithic disc more closely predicts the maximum value of stress but not at the actual position of occurrence. The monolithic disc model probably applies for single turn or helical disc type coils. The magnetic pressure method, although widely used, predicts for this coil a maximum stress of approximately one-half that measured and calculated by other methods. The measurement of a negative circumferential stress near the outside wall of the coil supports the conclusion of others that mechanical instability can be a problem in strip-wound coils. The difference between the floating shell theory and the measured stresses may be a result of transient effects in the magnetic field and current density; however, no consistent explanation has been developed. Another possible source of error is the effect which axial forces have on the circumferential stresses. These effects have been neglected. The type instrumentation employed in this study is used routinely and its performance is well known. A system error of approximately ± 5 per cent is suspected. The greatest error is likely to occur in reduction of data from the oscilloscope trace photographs. Other possible sources of instrumentation errors are: (1) transient response of the carrier amplifier, harmonic filter and oscilloscope, (2) measurement of the shunt calibration resistor, (3) measurement of the resistors and capacitors for the passive integrator, and (4) signal drift during acquisition of the calibration traces. To the knowledge of the writer, measurement of stresses within electromagnet windings has not been attempted before.

Transient diffusion effects certainly require further investigation. Of special interest should be the transient stresses at the conductor surface due to current density and magnetic field at the surface upon application of a short pulse voltage.

BIBLIOGRAPHY

BIBLIOGRAPHY

1. Hord, J. "Stress Analysis of Tape-Wound Magnet Coils," Journal of Research of the National Bureau of Standards, 69C:287-302, 1965.

2. Cockcroft, J. D. "The Design of Coils for the Production of Strong Magnetic Fields," Philosophical Transactions of the Royal Society, 227:317-343, May, 1928.

3. Daniels, J. M. "High Power Solenoids; Stresses and Stability," British Journal of Applied Physics, 4:50-54, February, 1953.

4. Giauque, W. F., and D. N. Lyon. "Design of a 100-kilogauss 4-Inch Core Solenoid for Continuous Operation," The Review of Scientific Instruments, 31:374-390, April, 1960.

5. Bitter, F. "Water Cooled Magnets," The Review of Scientific Instruments," 33:342-349, March, 1962.

6. Furth, H. P., and others. "Production and Use of High Transient Magnetic Fields. II," The Review of Scientific Instruments, 28:949-958, November, 1957.

7. Gersdorf, R., and others. "Design of High Field Magnet Coils for Long Pulses," The Review of Scientific Instruments, 36:1100-1109, August, 1965.

8. Ignatchenko, V. A., and M. M. Karpenko. "The Production of Constant Ultrahigh Magnetic Fields," Soviet Physics: Technical Physics, 13:143-146, July, 1968.

9. Carden, P. O. "Mechanical Stresses in Bonded Plane Helical Solenoids with Arbitrary External Field," Journal of Scientific Instruments, Series 2, 1:437-443, April. 1968.

10. Patterson, J. N. "Inductive Power Supply for a 100-inch Hotshot Wind Tunnel," Arnold Engineering Development Center TR-66-260, Arnold Air Force Station, Tennessee, March, 1967.

11. Woodson, H. H., and J. R. Melcher. Electromechanical Dynamics. Part II. New York: John Wiley and Sons, Inc., 1968.

12. Brown, G. V., and others. "Axial and Radial Magnetic Fields of Thick, Finite-Length Solenoids," National Aeronautics and Space Administration TR-R-170, Lewis Research Center, Cleveland, Ohio, December, 1963.

13. Brown, G. V., and L. Flax. "Superposition Calculation of Thick Solenoid Fields from Semi-Infinite Solenoid Tables," National Aeronautics and Space Administration TN-D-2494, Lewis Research Center, Cleveland, Ohio, September, 1964.

14. Timoshenko, S., and J. N. Goodier. Theory of Elasticity. New York: McGraw-Hill Book Company, Inc., 1951.

15. Timoshenko, S. Strength of Materials. Part II. Third edition. Princeton, New Jersey: D. Van Nostrand Company, Inc., 1956.

16. Durelli, A. J., and others. Analysis of Stress and Strain. New York: McGraw-Hill Book Company, Inc., 1958.

17. Montgomery, D. B. "High Field Magnets at the National Magnet Laboratory," Les Champs Magnetiques Intenses. Grenoble: Centre National de la Recherche Scientifique, 1966. Pp. 51-59.

18. Reitz, J. R., and F. M. Milford. Foundations of Electromagnetic Theory. Reading, Massachusetts: Addison-Wesley Publishing Company, Inc., 1960.

19. Pearson, A. "Note on Search Coil Errors in the Measurement of Axial Magnetic Fields," Journal of Scientific Instruments, 39:8-10, January, 1962.

APPENDIXES

APPENDIX A

DERIVATION OF THE MAGNETIC INDUCTION AT THE GEOMETRIC CENTER OF A THICK CYLINDRICAL MAGNET COIL

A generalized form of the Biot-Savart [18] law states that the magnetic induction $\vec{B}$ at position $\vec{r}_2$ due to a current I at position $\vec{r}_1$ is given by

$$\vec{B}\,(\vec{r}_2) = \frac{\mu_o}{4\pi}\, I \oint_c \frac{d\vec{\ell} \times (\vec{r}_2 - \vec{r}_1)}{|\vec{r}_2 - \vec{r}_1|^3} \quad , \tag{A-1}$$

where $d\vec{\ell}$ is an element of current conductor along the contour C. Consider the circular current filament of radius a as depicted in Figure 17. If the magnetic field is to be calculated at a point on the z-axis the following relations exist:

$$d\vec{\ell} = a d\theta\,(-\sin\theta\,\vec{e}_x + \cos\theta\,\vec{e}_y), \tag{A-2}$$

$$\vec{r}_2 - \vec{r}_1 = -\,a\cos\theta\,\vec{e}_x - a\sin\theta\,\vec{e}_y + z\,\vec{e}_z \;.$$

Substitution of Equations (A-2) into Equation (A-1) yields

$$\vec{B}(z) = \frac{\mu_o I}{4\pi} \int_o^{2\pi} \frac{(z\,a\cos\theta\,\vec{e}_x + z\,a\sin\theta\,\vec{e}_y + a^2\vec{e}_z)}{(z^2 + z^2)^{3/2}}\, d\theta$$

which, after integration, becomes

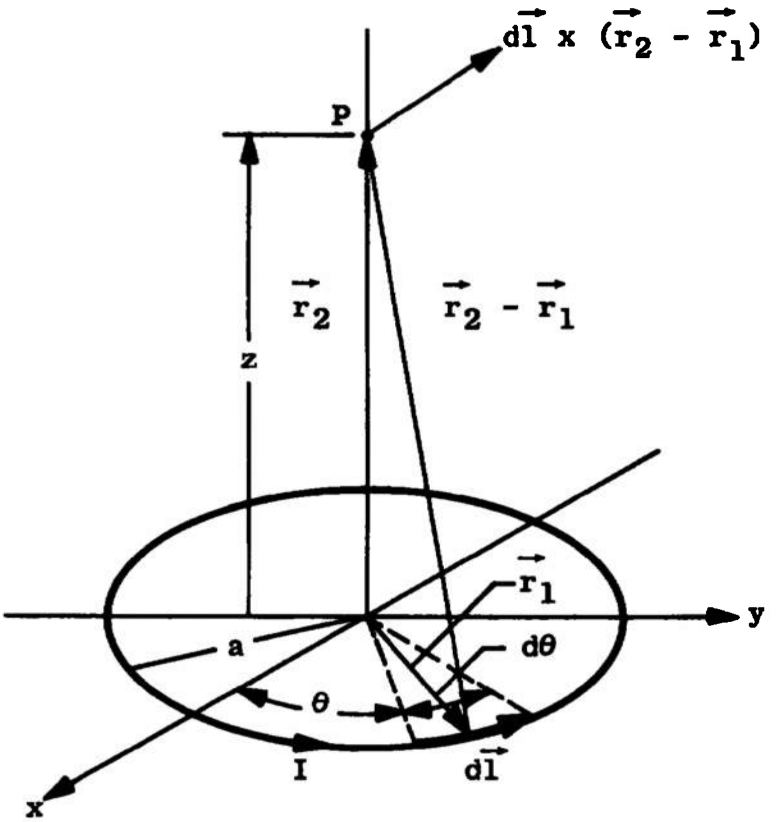

Figure 17. Axial magnetic field of a circular current filament.

$$\vec{B}(z) = \frac{\mu_o I}{2} \frac{a^2}{(z^2+a^2)^{3/2}} \vec{e}_z \,. \qquad \text{(A-3)}$$

Now, apply Equation (A-3) to each element dz of a cylindrical current sheet of radius a and length $2b$ as shown in Figure 18. If the sheet is uniformly wound with N_z turns, each element dz contains $N_z dz/2b$ turns; thus, the magnetic induction at point z_o is given by

$$B_z(z_o) = \frac{\mu_o N_z I}{2b} \frac{a^2}{2} \int_o^{2b} \frac{dz}{[(z_o-z)^2 + a^2]^{3/2}} \qquad \text{(A-4)}$$

Integration of Equation (A-4) yields

$$B_z(z_o) = \frac{\mu_o N_z I}{2b} \left(\frac{\sin \theta_2 - \sin \theta_1}{2} \right), \qquad \text{(A-5)}$$

where $\theta_1 = -\tan^{-1} (z_o/a)$ and $\theta_2 = \tan^{-1} (2b - z_o)/a$. At the geometric center of the coil $z_o = b$; thus, $\theta_1 = -\tan^{-1} (b/a)$ and $\theta_2 = \tan^{-1} (b/a)$. Making these substitutions into Equation (A-5) yields for the axial component of induction at the geometric center of the current sheet

$$B_z(0) = \frac{\mu_o N_z I}{2(a^2+b^2)^{1/2}} \,. \qquad \text{(A-6)}$$

Now, consider a thick coil make up of several concentric current sheets as depicted in Figure 19. Each element da contains $N_r da/(a_2-a_1)$ turns; thus,

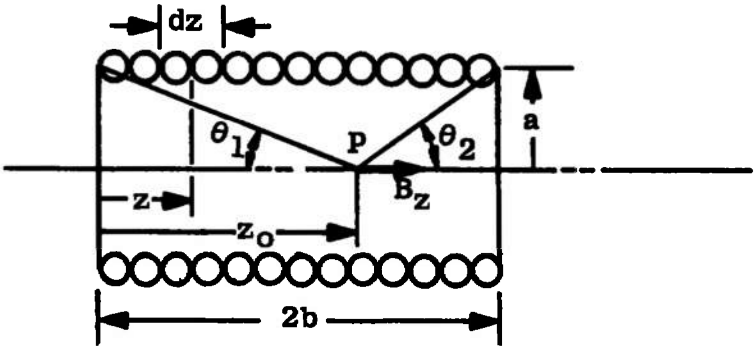

Figure 18. Axial magnetic field of a cylindrical current sheet.

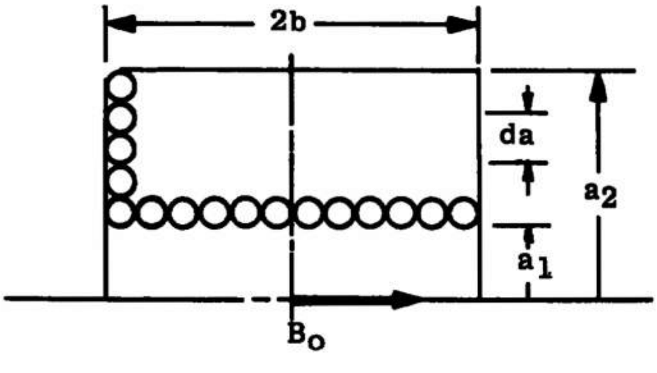

Figure 19. Axial magnetic field of a thick, finite length, cylindrical coil.

$$B_z(0) = \frac{\mu_o N_z N_r}{2(a_2-a_1)} \int_{a_1}^{a_2} \frac{da}{(a^2+b^2)^{1/2}} ; \qquad \text{(A-7)}$$

or,

$$B_z(0) = \frac{\mu_o N_z N_r}{2(a_2-a_1)} \ \ell n \left[\frac{a_2 + (a_2{}^2+ b^2)^{1/2}}{a_1 + (a_1{}^2+b^2)^{1/2}}\right]. \qquad \text{(A-8)}$$

Now, since $a_2/a_1 = \alpha$, $b/a_1 = \beta$, $\mu_o = 4 \times 10^{-7}$, and $N_z N_r = N$ = total number of turns, Equation (A-7) can be written as

$$B_z(0) = \frac{2\pi NI}{a_1(\alpha-1)} \ \ell n \left[\frac{\alpha + (\alpha^2 + \beta^2)^{1/2}}{1 + (1 + \beta^2)^{1/2}}\right] \times 10^{-7}. \qquad \text{(A-9)}$$

The magnetic field along the coil axis is purely axial; therefore, the magnetic induction at the geometric center of the coil is written as

$$B_o = \frac{NI}{2b(\alpha-1)} \left(\frac{2\pi\beta}{5}\right) \ell n \left[\frac{\alpha + (\alpha^2 + \beta^2)^{1/2}}{1 + (1 + \beta^2)^{1/2}}\right] \times 10^{-6}. \qquad \text{(A-10)}$$

APPENDIX B

DERIVATION OF AN APPROXIMATE EXPRESSION FOR THE RADIAL COMPONENT OF MAGNETIC INDUCTION FOR A THICK CYLINDRICAL MAGNETIC COIL

Since the radial magnetic field of a thick cylindrical coil carrying uniform current density is approximately sinusoidal across the radial dimension, Hord [1] suggests that the field distribution can be approximated by an expression of the form

$$\frac{B_r}{B_o} = K_o + (\hat{K} - K_o)\sin\pi\left(\frac{\gamma-1}{\alpha-1}\right). \tag{B-1}$$

where for each point along the coil axis

$$K_o = \frac{1}{2}\left[\left(\frac{B_r}{B_o}\right)_{\gamma=1} + \left(\frac{B_r}{B_o}\right)_{\gamma=\alpha}\right]$$

and $\hat{K}$ is the peak value of B_r/B_o. Values of B_r/B_o for any finite coil have been computed and tabulated [12,13]. By plotting several values of K_o and $K_o-\hat{K}$ versus z/b a linear approximation can be made by;

$$K_o = m_1\ z/b, \quad \hat{K} - K_o = m_2\ z/b, \tag{B-2}$$

where m_1 is the slope of the K_o versus z/b plot and m_2 is the slope of the $(\hat{K} - K_o)$ versus z/b plot for a given coil geometry. Substituting Equation (B-2) into Equation (B-1) yields

$$\frac{B_r}{B_o} = \frac{z}{b}\left[m_1 + m_2\sin\pi\left(\frac{\gamma-1}{\alpha-1}\right)\right]. \tag{B-3}$$

As pointed out by Hord [1], Equation (B-3) is valid everywhere within the volume occupied by the coil winding; also, the approximation is closest at the coil end planes where maximum compressive force is generated.

Figure 20 shows a plot of K_o versus z/b and $\hat{K} - K_o$ versus z/b for the experimental coil described in Chapter IV. Values of K_o and $\hat{K} - K_o$ were determined from the radial field plot in Figure 12, page 36. From Figure 20 values of m_1 and m_2 are found to be 0.285 and 0.194, respectively.

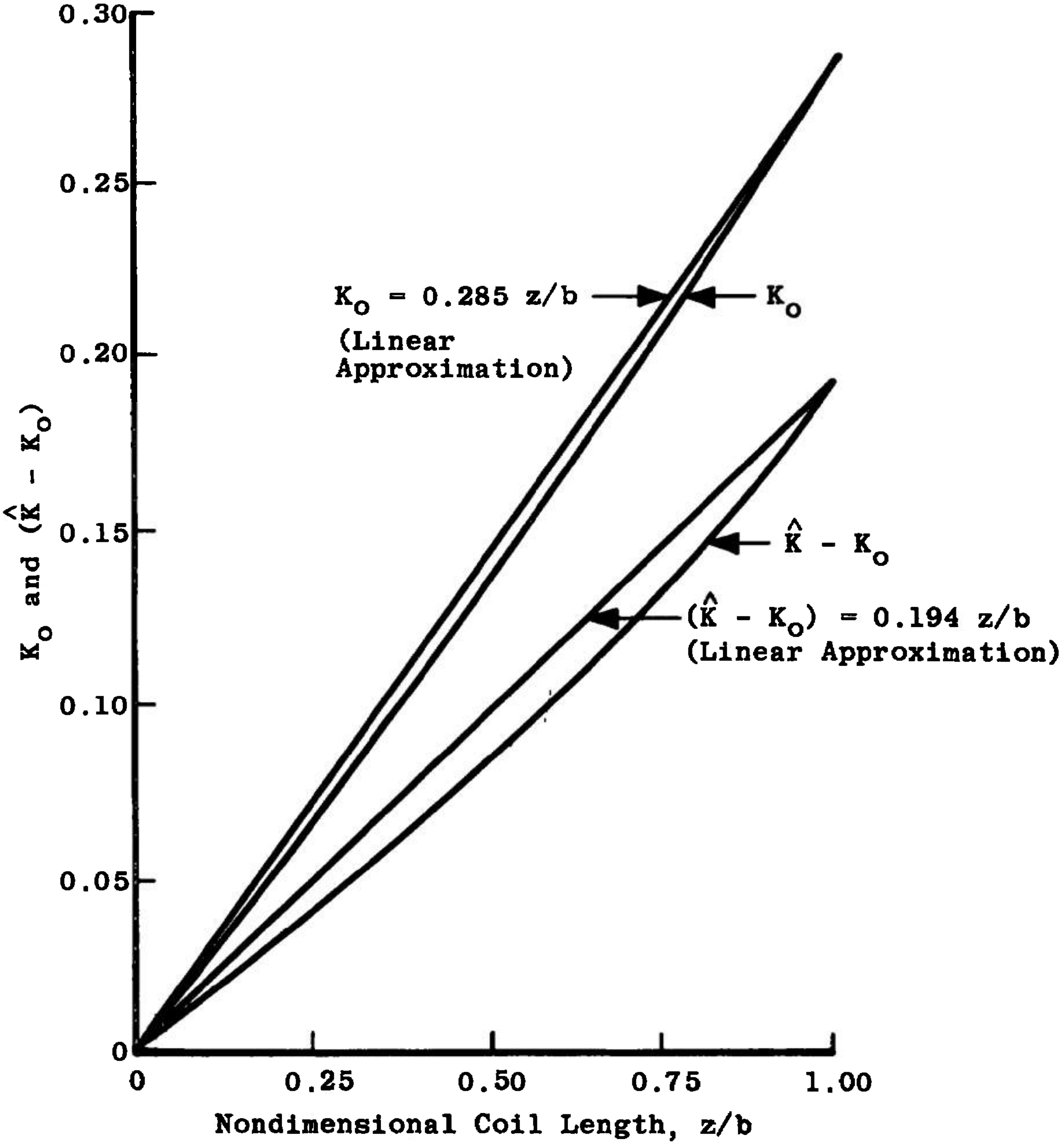

Figure 20. Plot of K_o and $(\hat{K} \quad K_o)$ versus z/b for the experimental magnet.

APPENDIX C

INSTRUMENTATION

In order to determine experimentally the distribution of the circumferential stress component across the radial dimension of the experimental coil several resistance type strain gages were bonded to the current conductor at different radial positions during the winding process. The gages used were William T. Bean type EA-09-250BK-10C which is a foil gage with an epoxy film backing. The bonding agent was Eastman type 910 contact cement. Each gage was mounted astride the coil midplane so as to sense the maximum circumferential strain at that particular radial position. A small cylindrical search coil was positioned coaxially inside the magnet coil and astride the midplane to sense the magnetic induction at the geometric center of the magnet.

A Tektronix, Incorporated Model 502 dual beam oscilloscope equipped with a Tektronix Series 125 Land type camera was used for recording simultaneously the strain and the magnetic induction signals. Both signals were half-sine pulses of approximately 5.8 milliseconds duration.

Strain Measurements

The manner in which the resistance of a strain gage varies with applied strain is given approximately by Poisson's ratio as

$$\Delta R_g = R_g\left(\frac{\Delta L}{L}\right)(G.F.), \qquad (C-1)$$

where ΔR_g is the incremental change of gage resistance R_g, $\Delta L/L$ is the unit strain to which the gage is subjected, and G.F. is the gage factor which varies with the type of gage. Since the unit strain $\varepsilon = \Delta L/L$, Equation (C-1) can be written as

$$\varepsilon = \frac{\Delta R_g}{R_g(G.F.)} \quad . \tag{C-2}$$

Thus, by measuring the change in resistance of the gage, the strain may be determined.

Consider a strain gage with resistance R_g connected in one arm of a Wheatstone bridge as indicated in the following sketch.

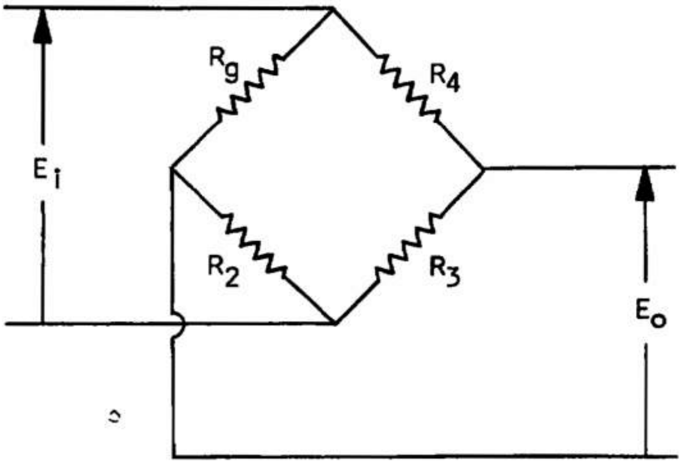

Wheatstone Bridge

If the bridge is excited with a voltage E_i, the output voltage is given by

$$E_o = \frac{E_i\ (R_gR_3 - R_2R_4)}{(R_g+R_2)(R_3+R_4)} \quad . \tag{C-3}$$

Let the gage be subjected to a strain ε so that R_g becomes $R_g + \Delta R_g$. Equation (C-3) then becomes

$$E_o = E_i \left[\frac{(R_g+\Delta R_g)R_3 - R_2R_4}{(R_g+\Delta R_g+R_2)(R_3+R_4)} \right] \quad . \tag{C-4}$$

Now, if $R_g = R_2 = R_3 = R_4 >> \Delta R_g$, then, to a close approximation,

$$E_o = \frac{E_i}{4} \left(\frac{\Delta R_g}{R_g} \right) . \tag{C-5}$$

Combining Equations (C-2) and (C-5) yields

$$E_o = \frac{E_i}{4} (\varepsilon)\ (G.F.)\ . \tag{C-6}$$

Thus, the output voltage of the bridge is directly proportional to the strain to which the gage is subjected.

In order to discriminate between the strain, signal and the voltage appearing due to electromagnetic induction, a carrier amplifier system was used for strain measurement. A schematic diagram of the system is shown in Figure 14, page 39. The amplifier used was a Consolidated Electrodynamics Corporation (CEC) Type I-127 which provides a 5 volt, 20 K Hz, carrier signal for bridge excitation. In the CEC

Type I-127 amplifier the output of the demodulator consists of the information signal plus the harmonics of the carrier frequency generated by the rectification action of the demodulator. An internal filter partially suppresses the harmonics; however, it was necessary to use an additional filter between the carrier amplifier and the oscilloscope in order to obtain a desirable signal to noise ratio. An active, fourth order, Gaussian to 6 db, transitional filter having a 2000 Hz half-power point was used. A schematic diagram of the filter is shown in Figure 21. A Fourier analysis shows that all components of a five millisecond half-sine pulse above 1000 Hz are negligible; therefore, no significant loss of signal can be attributed to the filter.

Magnetic Induction Measurements

According to Faraday's law of electromagnetic induction the electromotive force E associated with a change in magnetic flux Φ through a circuit of N turns is given [18] by

$$E = -N \frac{d\Phi}{dt} . \qquad \text{(C-7)}$$

By definition

$$\Phi = \int_S \vec{B} \cdot \vec{n} \, da; \qquad \text{(C-8)}$$

where S is the surface bounded by the circuit. Therefore, Equation (C-8) can be written as

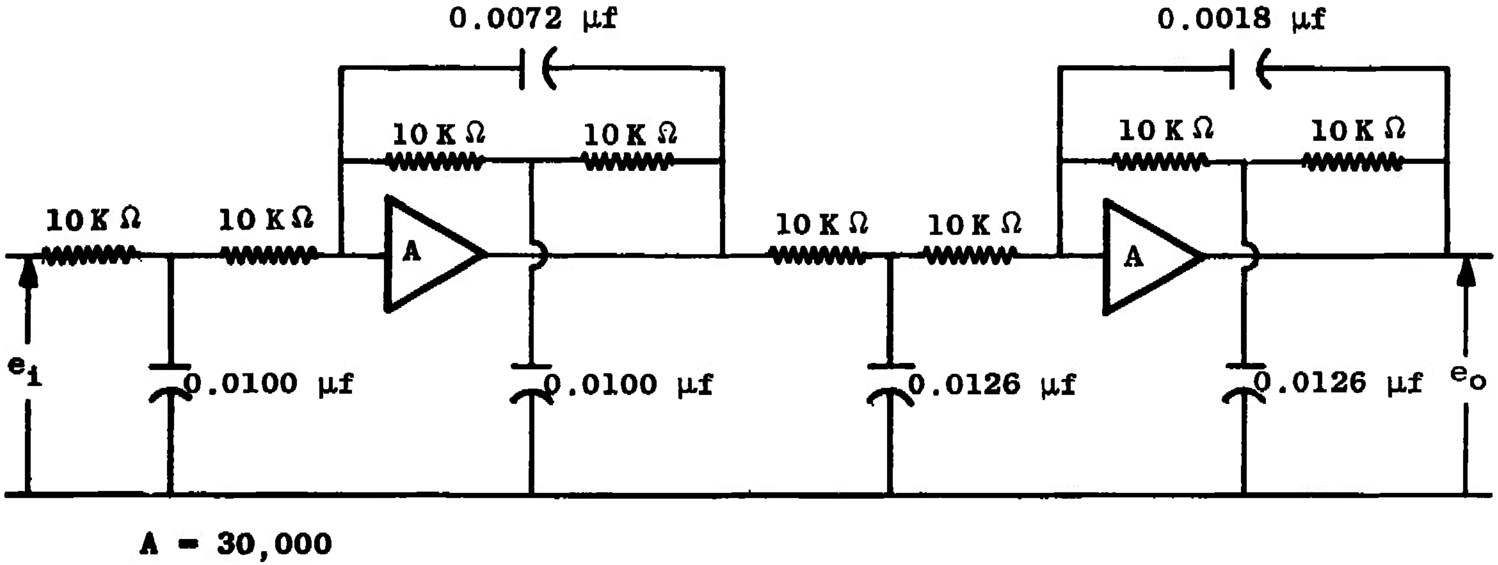

Figure 21. Schematic diagram for a four-pole, active, Gaussian to 6db, transitional filter.

$$E = -N \frac{d}{dt} \int_S \vec{B} \cdot \vec{n} \, da \qquad \text{(C-9)}$$

If the circuit is rigid and stationary the time derivative can be taken inside the integral where it becomes a partial time derivative; thus,

$$E = -N \int_S \frac{\partial \vec{B}}{\partial t} \cdot \vec{n} \, da \qquad \text{(C-10)}$$

Since this must be true for all surfaces S, it follows that

$$E = -NA \frac{\partial \vec{B}}{\partial t}, \qquad \text{(C-11)}$$

where A is the area of the surface. If the circuit is located in a magnetic field such that $\vec{B}$ is a function of time only, Equation (C-11) may be written as

$$E(t) = -NA \frac{d\vec{B}(t)}{dt}. \qquad \text{(C-12)}$$

In the above discussion it has been assumed that all N turns of the circuit experience an equal number of flux linkages, which cannot always be the case. However, it has been shown [19] that for a circuit consisting of a cylindrical coil of length 2b, inside radius a_1 and outside radius a_2, the error due to unequal flux linkages is negligible if the following relationship exists:

$$b^2 = \frac{a_2{}^3 - a_1{}^3}{4(a_2 - a_1)} \quad . \tag{C-13}$$

Now consider the RC network shown in the following sketch.

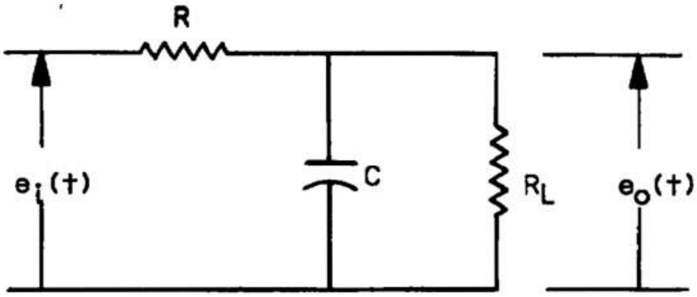

Passive Integrator

The frequency domain transfer function of the network is

$$\frac{E_o\ (\omega)}{E_i\ (\omega)} = \frac{\dfrac{R_L}{R + R_L}}{\dfrac{j\omega CRR_L}{R + R_L} + 1} \quad . \tag{C-14}$$

In the steady-state, at frequencies for which $j\omega CRR_L/R + R_L >> 1$, Equation (C-14) may be expressed as

$$e_o(t) = \frac{1}{RC} \int_0^t e_i(t)\ dt \tag{C-15}$$

where $1/j\omega = \int dt$. If the input to the RC network is the search coil output voltage given by Equation (C-12), the network output voltage is

$$e_o(t) = \frac{1}{RC}\int_o^B \left[-NA\,\frac{d\vec{B}(t)}{dt}\right]dt\ . \qquad \text{(C-16)}$$

Integrating and solving for B(t) yields

$$\vec{B}(t) = -\frac{RC}{NA}\,e_o(t)\ . \qquad \text{(C-17)}$$

The search coil for the experimental magnet was constructed of 126 turns of American Wire Gauge Number 44 film insulated copper wire wound on a cylindrical bobbin. A balanced differential integrator was used to eliminate common mode error signals. An RC time constant of 0.1 second was selected. The output of the integrator was displayed on the oscilloscope simultaneously with the strain signal. The induction measuring system is shown schematically in Figure 22.

Data Reduction

Determination of numerical values of strain from the strain signal photographs was accomplished by use of a shunt calibration procedure. Consider a strain gage with resistance R_g attached to a member to be tested and connected into a measuring system as indicated in the following sketch.

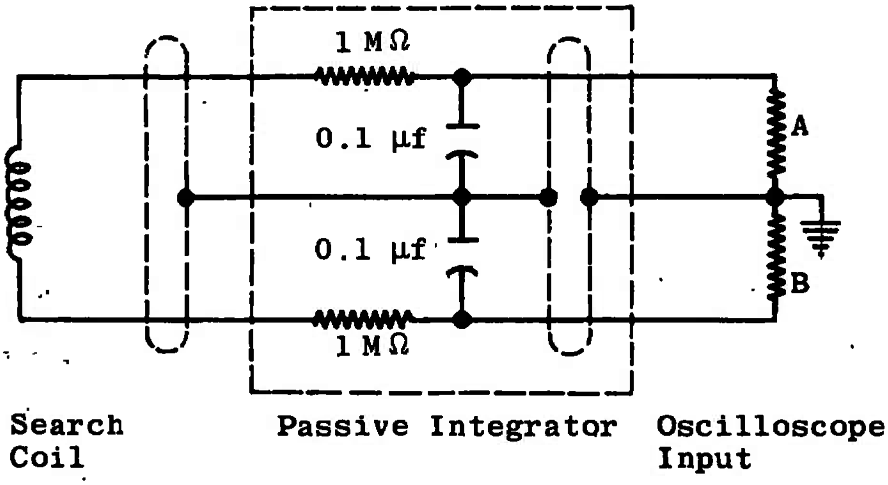

Figure 22. Schematic diagram of system for measuring magnetic induction.

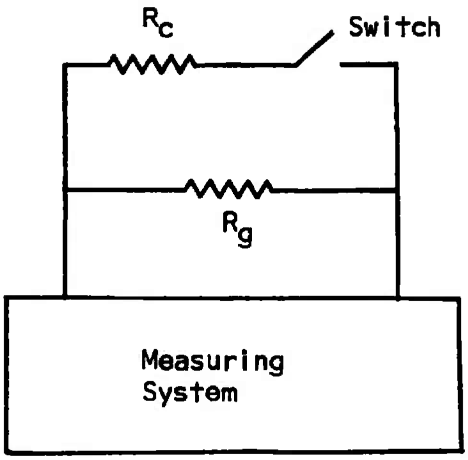

Shunt Calibration System

The gage is under constant or zero strain; therefore, the resistance seen by the circuit is R_g. If a calibrating resistor R_c is shunted across R_g, the equivalent resistance R_e presented to the measuring circuit is

$$R_e = \frac{R_g R_c}{R_g + R_c} . \tag{C-18}$$

The resistance change which has been affected is

$$\Delta R_g = R_g - R_e \quad \frac{R_g^2}{R_g + R_c} . \tag{C-19}$$

In order to produce such a resistance change in terms of strain, the gage must be subjected to a strain ε such that

$$\Delta R_g = \varepsilon(R_g)(G.F.) \qquad \text{(C-20)}$$

Therefore, the output indication obtained from the system by artificial means corresponds to an actual strain of

$$\varepsilon = \Delta R_g \times \frac{1}{(R_g)(G.F.)} \, . \qquad \text{(C-21)}$$

Combining Equations (C-19) and (C-21) results in an expression for the simulated strain ε_s in terms of known parameters; that is,

$$\varepsilon_s = \frac{R_g}{R_g + R_c} \times \frac{1}{G.F.} \, . \qquad \text{(C-22)}$$

By double exposure of the film, a reproduction of the oscilloscope traces for two different conditions may be displayed on one photograph. First, with the bridge excited and the gage subjected to no strain, a zero trace may be obtained. Then, by shunting the gage with a calibration resistor, a trace corresponding to the simulated strain is obtained. The displacement d_s between the two traces corresponds to the simulated strain given by Equation (C-22). Therefore, the actual strain from a data photograph is given by

$$\varepsilon = \varepsilon_s \frac{d}{d_s} \left[\frac{R_g}{R_g + R_c} \times \frac{1}{G.F.} \right] \times k_l \qquad \text{(C-23)}$$

where d is the trace deflection due to actual strain and k_l is the oscilloscope sensitivity constant. Corresponding values of stress were computed by use of the fundamental relationship between stress and strain given by

$$\sigma = \varepsilon E , \tag{C-24}$$

where E is Young's modulus of elasticity and σ is the stress.

Values of magnetic induction at the geometric center of the magnet coil corresponding to peak values of strain were determined by use of the relationship

$$B_o = \frac{RC}{NA} (d)(k_2) , \tag{C-25}$$

where RC is the integrator time constant, N is number of turns in the search coil, A is the effective area encompassed by the search coil, d is the signal trace deflection on the photograph, and k_2 is the oscilloscope sensitivity constant.

DOCUMENT CONTROL DATA - R & D

(Security classification of title, body of abstract and indexing annotation must be entered when the overall report is classified)

1. ORIGINATING ACTIVITY *(Corporate author)* Arnold Engineering Development Center ARO, Inc., Operating Contractor Arnold Air Force Station, Tennessee	2a. REPORT SECURITY CLASSIFICATION UNCLASSIFIED 2b. GROUP N/A

3. REPORT TITLE
EXPERIMENTAL VERIFICATION OF MAGNET COIL ANALYTICAL MODELS

4. DESCRIPTIVE NOTES *(Type of report and inclusive dates)*
November 1968 to February 1969 - Final Report

5. AUTHOR(S) *(First name, middle initial, last name)*
R. F. Carter, ARO, Inc.

6. REPORT DATE March 1970	7a. TOTAL NO. OF PAGES 84	7b. NO. OF REFS 19

8a. CONTRACT OR GRANT NO. F40600-69-C-0001 b. PROJECT NO. 7778 c. Program Element 63101F d. Task 777807	9a. ORIGINATOR'S REPORT NUMBER(S) AEDC-TR-69-264 9b. OTHER REPORT NO(S) *(Any other numbers that may be assigned this report)* N/A

10. DISTRIBUTION STATEMENT
This document has been approved for public release and sale; its distribution is unlimited.

11. SUPPLEMENTARY NOTES Available in DDC	12. SPONSORING MILITARY ACTIVITY Arnold Engineering Development Center, Air Force Systems Command, Arnold AF Station, Tenn. 37389

13. ABSTRACT

In this study of the elastic stresses in thick, strip-wound magnet coils experimental data are compared with theoretical stresses based on three physical models. It is shown that the floating shell model predicts radial dependence of the circumferential stresses produced by the J x B body forces better than the monolithic disc or magnetic pressure models. The fundamental equations relating the magnetic body forces to the stresses in the conductors are derived from first principles. The instrumentation for measuring stresses within magnet windings is described. A survey of several recent magnet stress studies is included.

14. KEY WORDS	LINK A		LINK B		LINK C	
	ROLE	WT	ROLE	WT	ROLE	WT
magnetic coils stresses elastic properties elastic theory tests						

17-5

AFSC
Arnold AFS Tenn